Chapter 8
Nanostructured Steels

Rosalia Rementeria, Carlos Capdevila, and Francisca G. Caballero

Abbreviations

APT	Atom probe tomography
ARB	Accumulative roll bonding
CCGT	Combined cycle gas turbine
CVD	Chemical vapor deposition
DED	Direct energy deposition
DLP	Direct in-line patenting
DP	Direct patenting
ECAP	Equal channel angular pressing
ED	Easy drawable
GAR	Grain aspect ratio
GARS	Gas atomization reactive synthesis
HAGB	High-angle grain boundaries
HPT	High-pressure torsion
LAGB	Low-angle grain boundary
LM	Liquid metal
LMP	Larson-Miller parameter
MA	Mechanical alloying
MBE	Molecular beam epitaxy
MF	Multiaxial forging

R. Rementeria (✉)
Additive Manufacturing – New Frontier, ArcelorMittal Global R&D, Avilés (Asturies), Spain
e-mail: rosalia.rementeria@arcelormittal.com

C. Capdevila · F. G. Caballero
Physical Metallurgy Department, National Centre for Metallurgical Research (CENIM-CSIC), Madrid, Spain
e-mail: ccm@cenim.csic.es; fgc@cenim.csic.es

R. Rana (ed.), *High-Performance Ferrous Alloys*,
https://doi.org/10.1007/978-3-030-53825-5_8

NFA	Nanostructured ferritic alloy
ODS	Oxide dispersion strengthened
PM	Powder metallurgy
PVD	Physical vapor deposition
RFCS	Research fund for coal and steel
SEM	Scanning electron microscopy
SFR	Sodium-cooled fast reactor
SLM	Selective laser melting
SPD	Severe plastic deformation
TE	Tensile elongation
TEM	Transmission electron microscope
TMT	Thermomechanical treatment
UFG	Ultrafine-grained materials
UTS	Ultimate tensile strength
XRD	X-ray diffraction

Symbols

A_{c3}	Temperature of the $\gamma/(\alpha+\gamma)$ phase boundary detected upon heating
A_{cm}	Temperature of the $\gamma/(\gamma+\theta)$ phase boundary detected upon heating
Ae'_3	Temperature of the $(\alpha+\gamma)/\gamma$ paraequilibrium phase boundary
Ae''_3	Temperature of the $(\alpha+\gamma)/\gamma$ paraequilibrium phase boundary allowing for the stored energy in ferrite
B_S	Bainite start temperature
d_p	Size of precipitates
G	Shear modulus of the material
k	Constant
$\overline{L}$	Mean lineal intercept as a measure of the effective grain size
M_S	Martensite start temperature
N_p	Number density of precipitates
P	Average die pressure
Q	Heat of formation per unit mass
So	Interlamellar spacing
t	Bainitic ferrite plate thickness
T	Temperature
T_e	Eutectoid temperature
T_M	Melting temperature
T_0	Temperature at which austenite and ferrite of the same chemical composition have identical free energy
T'_0	Temperature at which austenite and ferrite of the same chemical composition have identical free energy and the strain term for ferrite is incorporated
V_α	Volume fraction of ferrite
$V_{\gamma,0}$	Initial volume fraction of retained austenite

V_γ	Volume fraction of retained austenite
$x'_{\gamma\alpha}$	Carbon content of austenite given by $(\alpha + \gamma)/\gamma$ paraequilibrium phase boundary
x'_{T_0}	Carbon content of austenite at the T'_0 curve
α	Ferrite
ΔG	Gibbs free energy
ε	Strain
ε_p	True plastic strain
γ	Austenite
μ	Average coefficient of friction
ρ	Density
σ_ρ	Dislocation forest strengthening
σ_d	Drawing stress
σ_{HP}	Hall-Petch strengthening
σ_p	Nano-oxide precipitation strengthening
σ_Y	Yield strength

8.1 Introduction and Definitions

Since Herbert Gleiter (the founding father of nanotechnology) in the 1980s [170, 190], the field of nanomaterials has flourished over the last three decades due to its scientific and technological importance. Gleiter's basic idea was formulated and explored experimentally in a 1981 paper on "materials with ultra-fine grain sizes" [84], where he announces a new class of materials referred to as "interfacial" or "microcrystalline", not using yet the term "nanocrystalline materials." Nevertheless, Gleiter's description of these new materials meets the definition of nanotechnology owing to nanoscale-dependent material properties. According to his first ideas, the atoms in the boundary or interface region of a nanometer scale domain can adjust their positions in order to increase the strength and decrease the energy of the boundary, irrespective of the usual constraints from the volume or bulk of a material. In addition, Gleiter foresees that the structure and properties of the material having a volume of interfaces comparable or larger than the volume of crystals may be different from the structure and properties of the crystalline state of the same material.

The mechanical and physical properties of steels are determined by several parameters, namely the intrinsic strength of pure annealed iron, solid solution strengthening and various microstructural components including particle or precipitation contributions, dislocation strengthening and grain size effects. Among them, the average grain size of the material generally plays a very significant and, often, dominant, role. The dependence of strength on grain size is expressed in terms of the Hall-Petch equation for equiaxed structures [92, 188], strength depending on $\overline{L}^{-1/2}$, where $\overline{L}$ is the mean lineal intercept as a measure of the *effective grain size*. In the case of lath or plate-shaped grains, such as those of bainite and martensite, strength depends on $\overline{L}^{-1}$ [163, 169]. It was predicted that in nanostructured steels resistance

to plastic deformation by dislocation motion would steadily increase as grain size is reduced [82]. This proved to be true, except that nanocrystalline grain sizes of certain metals produce often "negative or inverse Hall-Petch effect", not observed in the particular case of iron-based materials [37, 45].

The term "nanostructured materials", with "nanocrystalline materials" and "nanophase materials" as backups, has become a generic reference to a wide range of grain and precipitate structures. In order to provide a rationalized and simple classification, *nanostructured materials* are here defined to represent cases where the governing lengthscale $\overline{L}$ is below 100 nm, as opposed to *nanocrystalline materials*, which are those with crystallite sizes smaller than 100 nm. Materials whose governing lengthscale lies within the sub-micrometer scale (100 nm–1 μm) are termed *submicron materials*, while more generically, the term *ultrafine-grained materials* (UFG) is used to refer to both nanostructured and submicron materials. In order to qualify as *bulk nanostructured materials*, the condition to fulfill is that they can be manufactured in parts which are *large* in all three dimensions, with uniform properties throughout. The definition of large depends on the eye of the beholder; for this chapter, large is big enough to produce a technologically relevant component.

The techniques used nowadays to produce bulk nanostructured materials are usually divided into two categories, i.e., the *top-down* and the *bottom-up* approaches [255], to which a third *middle-out* approach can be added. In the *top-down* approach, a bulk solid with a relatively coarse grain size is processed to produce an UFG microstructure, often submicron and sometimes nanoscale, through severe plastic deformation. In the *bottom-up* approach, nanostructured materials are fabricated by assembling individual atoms or by consolidating nanoscale solids. The *middle-out* approach does not involve any mechanical operation or chemical reaction; nanostructures are obtained by solid-solid phase transformations through controlled heat treatment.

This chapter provides an overview of the most relevant and promising processing strategies to produce nanostructured steels and the structures and related properties thus obtained. These are nanostructured pearlitic wires obtained by severe plastic deformation, nanostructured ferritic steels produced by mechanical alloying and nanostructured pearlitic and bainitic steels formed by solid reaction.

8.2 Processing and Design of Bulk Nanostructured Steels

8.2.1 Nanostructured Steels Produced by Severe Plastic Deformation

The benefits of heavily deformed steels have been known to humankind for more than three millennia. It is a fact that technological progress in metallurgy has first benefitted the development of weapons, from daggers to cannons, and that this

development has been led by the know-how and fighting techniques across the ages and civilizations. The earliest examples of steels subjected to severe plastic deformation can be found in slashing and stabbing weapons, such as swords, glaives, sabers and daggers, discovered in archeological excavations. For instance, the Persian Damascus blades made from wootz steel were known to be the finest weapons produced in Eurasia and were reputed to cut even silk [221]. The exact processing technique of Damascus steel is still shrouded in mystery, but it is thought that small hockey puck-sized high-carbon steel ingots were forge-welded together by hammering at a temperature close to or above Ac_m, producing a flat strip, which is repeatedly folded and re-forged, each fold doubling the number of layers contained through-thickness [258]. Although the final microstructure has been found to contain cementite nanowires encapsulated by carbon nanotubes [196], shown in Fig. 8.1, the structure of the matrix remains micrometric. An overview of the metallurgy and microstructures of antique weapons is given in [58].

Nowadays, hypereutectoid nanopearlitic steel wires produced by drawing have the highest strength of all mass-produced steel materials, reaching tensile strengths above 6 GPa [135]. These are used for a wide variety of applications including, but not limited to, steel cords for reinforcing automobile tires, galvanized wires for suspension bridges and piano wires.

In the case of wire drawing, grain size reduction is accumulated through the reduction in the cross-section area. Alternative processes have been developed in which the overall dimensions of the workpiece remain practically unchanged after each deformation cycle, so that nanostructures are obtained by repetitive cyclic plastic deformation. The term *severe plastic deformation* (SPD) is frequently reserved to refer to processes which do not involve a net change of shape. However, the steel industry is conservative to adapt any of the net-shape SPD processes, primarily due to cost and scalability factors.

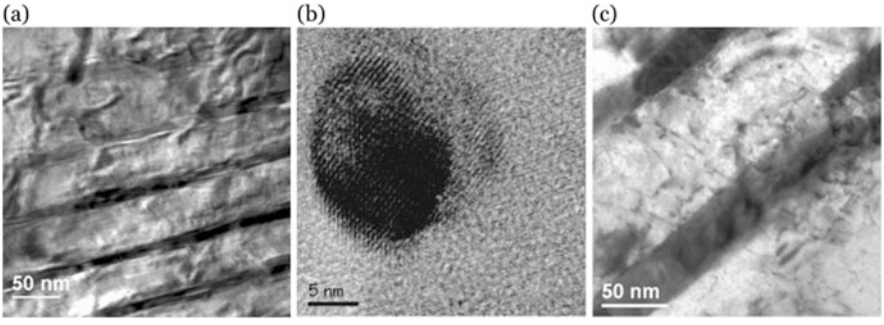

Fig. 8.1 (**a**) Bright-field transmission electron microscope (TEM) image of cementite nanowires in a Damascus sabre; the dark stripes indicate wires of several hundreds of nanometers in length, (**b**) high-resolution TEM image of the cross section of a cementite nanowire piercing the image plane and (**c**) bright-field TEM image of dislocation lines tangled at cementite nanowires. Reprinted with permission from Springer Nature: Springer Physics and Engineering of New Materials, Discovery of Nanotubes in Ancient Damascus Steel, Reibold et al. [196]

8.2.1.1 Heavily Deformed Pearlite Wires

Drawing operations involve pulling a wire, rod or bar (usually having a circular cross-section) through a die or converging channel to decrease its cross-sectional area and increase length. Wire drawing is produced by the combination of a pulling force and a pressure force from the die, which extends the wire and reduces its cross-sectional area while passing through the die, as schematized in Fig. 8.2. The combined effect of this drawing force should be less than the force that would cause the wire to stretch, neck, and break downstream from the die. Also, a too large reduction in cross-sectional area might break the wire. In industrial practice, pulling loads are rarely above 60% of the as-drawn strength, and the area reduction in a single drawing pass is rarely above 30% or 35% and is often much lower [270].

The reason why drawing cannot be achieved by simply stretching the wire with a pulling force is the necking phenomenon. Essentially, after a certain amount of uniform reduction in cross-sectional area, all further elongation concentrates at a single location or neck, which rapidly stretches and breaks. A heavily drawn wire has little or no work-hardening capability and immediately necks when subjected to simple stretching. Die-less drawing systems based on simple stretching are of limited application because of necking vulnerability of heavily drawn steels, and heating of the system is required [109].

In pearlitic steels, the starting microstructure for wire production is critical, and a previous heat treatment, termed patenting, is needed. Patenting consists of heating above Ac_3 or A_{cm}, followed by either continuous cooling or isothermal holding to produce a uniform and fine pearlite microstructure. In this sense, the work hardening rate during drawing and the delamination resistance are enhanced through elimination of upper bainite in the microstructure [171]. Figure 8.3 shows an isothermal transformation diagram for an eutectoid steel and the relevant transformation products as a function of the temperature, where the range to produce the desired fine pearlitic microstructure for wire drawing is indicated [172]. The temperature at which the patenting treatment is performed has a pronounced effect on the interlamellar spacing [248]. Coarse microstructures would give rise to

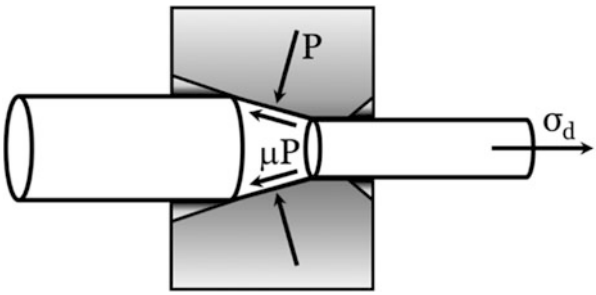

Fig. 8.2 Schematic illustration of the main forces in drawing, P is the average die pressure, μP is average frictional stress, where μ is the average coefficient of friction, and σ_d is the drawing stress

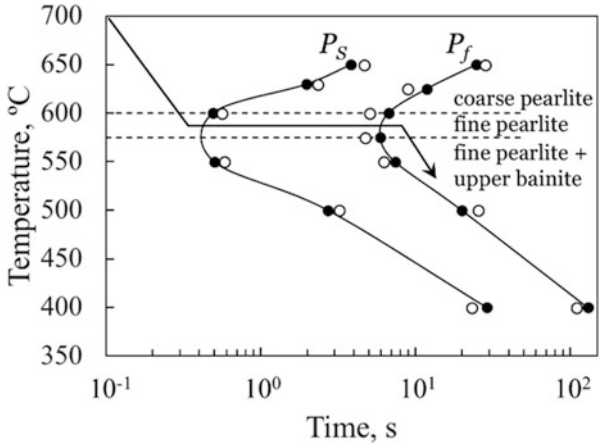

Fig. 8.3 Isothermal time-temperature-transformation diagram of a 0.8C-0.2Si-0.6Mn (wt.%) steel (hollow dots) and a 0.9C-0.2Si-0.3Mn-0.2Cr (wt.%) steel (filled dots) showing the transformation temperature range needed to produce fine pearlite by patenting. (Adapted from [126, 172])

brittleness if the material was left in the heat-treated condition, but this effect is not noticed after a few drawing passes. The patented wire is heavily strained by wet wire drawing to avoid heat generation [86].

Patenting may be applied to hot-rolled rods at the start of wire drawing or to cold-drawn wire as an intermediate heat treatment prior to further wire drawing. Fine pearlite has been traditionally produced in wires by isothermal transformation in molten lead baths (lead patenting). Alternative processing, such as Stelmor® or direct patenting (DP), easy drawable (ED) or direct in-line patenting (DLP) systems, have been developed to produce fine pearlite directly after hot rolling to rod in high-speed bar mills by controlled cooling processes [60, 176].

All carbon steel wire microstructures are prone to both static and dynamic strain aging. Static strain aging refers to the transient stress peaks observed in dilute alloys when a pre-strained specimen is unloaded and aged (even at room temperature) for a time and then reloaded with the same strain rate as in pre-straining. It is commonly accepted that the effect is related to the formation of Cottrell atmospheres around dislocations by diffusing solute atoms ageing [127, 263]. Dynamic strain ageing is the consequence of recurrent pinning of dislocations repeatedly arrested at obstacles to their motion in the process of straining. After a carbon steel wire has been in service or storage for a few months at ambient temperature, it is assumed to be fully strain aged. Static strain ageing may lead to the appearance of yield point phenomena, paneling and discontinuous yielding during further forming operations. Besides, dynamic strain aging is a major consideration during steel wire drawing, since the adiabatic heat produced by plastic deformation and the frictional heat generated between the dies and the wire rod result in deformation temperatures above 200 °C. The temperatures at which dynamic strain aging occurs during steel wire drawing are dependent on both the microstructure and the strain rate [81],

and they can be reasonably reached by the wire surface. In practice, the drawing speeds should be selected so as to minimize immediate static strain aging and avoid dynamic strain aging for the bulk of the wire cross section during drawing [126].

It is not surprising that large residual stresses are retained in the wires after heavy cold drawing. These depend strongly on the position in the wire; compressive stresses are found at the center and tensile stresses arise near the surface [210]. In an industrial context, stress relieving of cold drawn steel wires is performed at temperatures as low as 200 °C, in order to maximize strength and minimize stress relaxation. Alternatively, residual stresses can be relieved to a great extent by a stabilization thermomechanical procedure, i.e., by applying a plastic deformation on the wire surface, thus turning the tensile residual stresses into compressive ones [6].

8.2.1.2 Net-Shape Severe Plastic Deformation

Deforming steels to very large plastic strains without introducing any cracks is not a trivial task. Conventional processing of steel, such as forging or rolling, is carried out at relatively high temperatures where large strains are needed. In net-shape SPD processes, compressive hydrostatic stresses are present along with the shear stresses required for plastic deformation. Shear stresses impart the required plastic strains, while hydrostatic stresses prevent the samples from cracking. Given that SPD processes are cyclic, all of them should be such that at the end of any cycle the overall shape remains the same, ensuring that the process can be repeated again, thereby accumulating further plastic strain [116].

The most relevant net-shaped SPD processes for steels are equal channel angular pressing (ECAP) [5, 55, 68, 107], high pressure torsion (HPT) [67, 158, 202, 280] and multiaxial forging (MF) [141, 178, 236, 245, 276]. Steels produced by SPD processing such as ECAP, HPT, or MF processes usually have an average grain size between 0.2 and 0.5 μm, with a highly distorted crystal lattice. However, the crystallite size, or the size of the coherent domains, as determined from X-ray diffraction (XRD) analyses is of about 50 nm. Although not truly nanostructured materials, this technicality lets these SPD materials to be classified as nanocrystalline materials.

Accumulative roll bonding (ARB) [47, 48, 249] is a process suitable for large-scale production which involves the repeated rolling and folding of sheet material in order to accomplish strain increments without thinning the sample entering the rolls. However, the process does not lead to particularly fine grains, which tend to be closer to micrometers than nanometers in size.

Net-shape SPD has not demonstrated to be a relevant technology to produce bulk nanostructured steels and is left out of this chapter. Needless to say, this does not mean that further improvements in the processes, a finer control of the strain and temperature to which steels are subjected, and tailored alloy compositions could not lead to a new class of competitive bulk nanostructured steels. However, scalability and processing costs remain an unresolved issue.

8.2.2 Nanostructured Steels Produced by Mechanical Alloying

An alloy can be created without melting, by violently deforming mixtures of different powders [10, 91, 219]. This technique was developed around 1966 by Benjamin and his co-workers at the Inco Paul D. Merica Research Laboratory as a part of the program to produce oxide dispersion strengthened (ODS) Ni-based superalloys for gas turbine applications [13]. Nowadays, there are two main classes of mechanical alloys which are of commercial significance, the ODS iron-base superalloys and the ODS nickel-base superalloys. They all contain chromium and/or aluminum for corrosion and oxidation resistance, and yttrium or titanium oxides for creep strength. Yttrium oxide cannot be introduced into either iron or nickel by any method other than mechanical alloying; indeed, this was the motivation for the original work by Benjamin [13]. Since the topic of this book is on ferrous materials, the focus is put on iron-base ODS, and, hereafter, the term ODS will refer only to those with iron as solution matrix. Nanostructured ferritic alloys (NFAs) are a subcategory of ODS steels, characterized by ultrafine matrix grain size (200–400 nm) and an extremely high number density ($>10^{24}$ m^{-3}) of nanoclusters/nanoprecipitates (2–4 nm diameter) in the grain interiors and precipitates decorating the grain boundaries [153, 174].

ODS alloys are manufactured by mechanical alloying techniques involving powder metallurgy. This concept is understood to mean the refining of elementary or alloyed metal powders by high-energy milling. This results in alloy powders of extremely fine-grained structure, in which inert oxides, the dispersion particles responsible for boosting the strength of the material, and the alloying elements themselves are introduced uniformly into the microstructure. By means of hot compaction of the mechanically alloyed powder, the fully dense material is derived and this is then worked to create the semi-finished product. Semi-finished ODS superalloys are further processed to finished components by hot-forming methods, machining, or chip-less metal forming. Heat treatment then induces recrystallization, either into a coarse columnar grain structure or into a fine, equiaxed set of grains. The parts are then assembled by mechanical means (bolts or rivets) or by welding or brazing. A scheme of the typical processing route of ODS steels is presented in Fig. 8.4.

There are several potential advantages in employing ODS ferritic steels for high-temperature power plant applications: in addition to the lower raw material cost, the alloys have a higher melting point, lower density, and lower coefficient of thermal expansion than the current nickel- or cobalt-base alloys. However, the mechanical strengths of the alloys in the cast and wrought condition at temperatures in excess of about 600 °C were too low for them to be considered for critical structural applications. Dispersion strengthening with stable oxide particles is an ideal method for improving high temperature strength without sacrificing the excellent surface stability of the matrix alloy. Fe-based ODS alloys, such as MA956 and PM2000, have a composition and microstructure designed to impart creep and oxidation resistance in components operating at temperatures from ~1050 °C to 1200 °C and

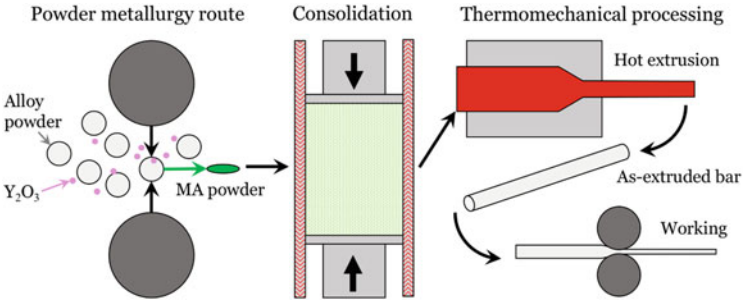

Fig. 8.4 Schematics of the processing route of ODS alloys

Table 8.1 Chemical composition (wt.%) of ODS steels and NFAs

Steel	Cr	Mo	W	Ti	Al	Dispersoid	Ref.
MA956	20	–	–	0.5	4.5	$0.50Y_2O_3$	[42]
MA957	14	0.3	–	1	–	$0.25\ Y_2O_3$	[42]
PM2000	19	–	–	0.5	5.5	$0.50\ Y_2O_3$	[122]
ODM 751	16.5	1.5		0.6	4.5	$0.50Y_2O_3$	[118]
12Y1	12					$0.25\ Y_2O_3$	[1]
12YWT	12	–	2.5	0.4	–	$0.25\ Y_2O_3$	[1]
14Y1	14					$0.25\ Y_2O_3$	[1]
14YWT	14	–	3	0.4	–	$0.25\ Y_2O_3$	[1]
14Cr CEA	14	–	1	0.3	–	$0.25\ Y_2O_3$	[63]

above. These alloys achieve their creep resistance from a combination of factors, i.e., the presence of a very coarse, highly textured, high grain aspect ratio (GAR) structure that results from and is sensitive to the alloy thermomechanical processing history [218], and the dispersion of fine scale (20–50 nm diameter) Y_2O_3 particles introduced during mechanical alloying that are highly stable to Ostwald ripening. NFAs typically contain $\geq$12 wt.% Cr along with tungsten and/or molybdenum for solid solution strengthening and ferrite stabilization, as well as small amounts of yttrium, titanium, and oxygen. NFAs are usually designated by their weight percentage of Cr content followed by YWT, as in 12YWT and 14YWT [29, 173]. Table 8.1 collects typical chemical compositions of ODS steels and NFAs.

8.2.2.1 Alternative Routes for Producing ODS Steels

The standard powder metallurgy (PM) route for the fabrication of ODS steels (including NFAs) involves several steps, such as gas atomization to produce a pre-alloyed powder, mechanical alloying (MA) with fine oxide powders, consolidation, and finally thermal/thermomechanical treatment (TMT). This fabrication route is complex and expensive, and the scale up for industrial production is very limited. The suitability of this family of steels for high temperature applications in harsh

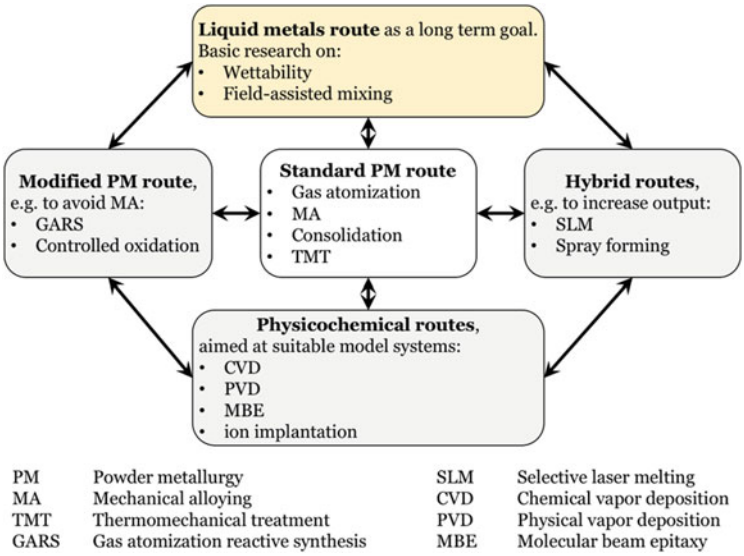

Fig. 8.5 Schematic classification of fabrication routes toward ODS steels conceptualized from [14]

environments [4, 88, 146, 177, 194, 235, 252] has led to a growing interest in complementary or alternative fabrication routes able for industrial scale-up offering a reasonable balance of cost, convenience, and properties. Bergner et al. [14] recently reviewed the most promising new routes toward ODS steels. Assuming the conventional PM/AM route as the benchmark for the fabrication of ODS steels, the focus is mainly put in hybrid routes that comprise aspects of both the PM route and more radical liquid metal (LM) routes as promising approaches for larger volumes and higher throughput of fabricated material. A summary of the alternative routes from the above research is shown in Fig. 8.5. The well-established and default processes for the production of ODS steels based on a PM route that depend on an extended MA step to reach an intimate mixture of oxides in a steel matrix requires quite extended alloying times (typically 60 h). The precipitation of the necessary high number density of oxide nanoparticles then occurs during consolidation, heat treatment, and any subsequent thermomechanical processing. In an attempt to avoid the extended and usually costly MA step, and to facilitate greater volumes of ODS material, a range of LM and hybrid routes have been developed nowadays, including ultrasonic dispersion of particles in the melt and in situ oxidation approaches based on atomization, spray forming, and melt spinning. Although none of the processes have reached a maturity where the competitiveness with PM/MA can be assessed, there is sufficient encouragement in early results to pursue alternatively manufactured ODSsteels. Regarding scalability, in terms of consolidation of powders along with hot isostatic pressing plus hot extrusion, spark plasma sintering and other similar field-assisted techniques have

now convincingly shown promise for scaling-up to an industrial frame. Given the importance of ODS alloys, particularly to the niche of energy-generating industry, and civil nuclear power in particular, it is necessary that alternative manufacturing techniques for small components, such as additive manufacturing technologies [56], are standardized.

8.2.3 Nanostructured Steels Produced by Solid Reaction

8.2.3.1 Nanostructured Pearlite

Pearlite, as the very first microstructure to be ever observed under a microscope, is probably the best understood among the solid-solid phase transformations in steels. However, quoting Robert's [150] paper on the structure and rate of formation of pearlite [150, 151], "no one could readily believe that the subject is exhausted, and there can be no doubt but that it will continue to interest the investigator for many years to come."

The course of the isothermal transformation of a steel after austenitization and further quenching to a temperature level above the martensite start temperature is conveniently represented by the so-called S curve or time-temperature-transformation (TTT) diagram. Figure 8.3 schematizes transformations taking place above the martensite start temperature (M_S) in low alloy steels, where two transformation products are distinguished: pearlite forming above the knee of the S curve and bainite forming below. It is well-known that the interlamellar spacing of pearlite decreases as the reaction temperature is lowered [184]. Back in the beginning of the twentieth century, when the resolution power of microscopes was limited, transformation products at large undercoolings near the knee of the S curve were not resolvable. Metallurgists thought that the pearlite nodules thus produced were indeed lamellar pearlite, but of an interlamellar spacing too small for the resolution of the metallurgical microscope [123, 124]. Zener's simple but yet useful thermodynamic approach can be used to illustrate the relationship between the interlamellar spacing and the transformation temperature in pearlitic steels. Under Zener's treatment, a pearlite nodule of interlamellar spacing So advances into the parent austenite, as illustrated in Fig. 8.6. As the nodule grows, the free energy remains unchanged in a region that includes one cementite and one ferrite plate (or two halves of ferrite plates at both sides of the cementite plate) with an interlamellar distance of S_0 and depth of W, as indicated by dotted lines in Fig. 8.6. As the nodule advances a distance dx, the volume of austenite transformed in the region under consideration is $S_0 W dx$, and the mass of the austenite transformed is $\rho S_0 W dx$, where ρ is the density. The free energy that is available at temperature T for the formation of new interfaces is given by

$$\Delta G = Q \frac{T_e - T}{T} \rho S_0 W dx \tag{8.1}$$

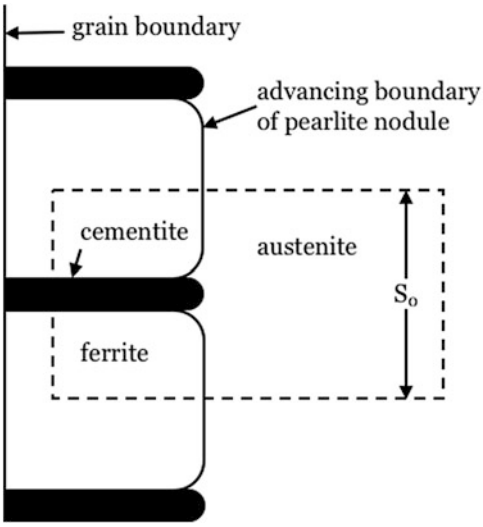

Fig. 8.6 Illustration of an advancing pearlite nodule

where Q is the heat of formation of pearlite per unit mass and T_e is the eutectoid temperature. Growth of the lamellae is possible only if the increase in the surface energy is outweighed by the increase of free energy resulting from the transformation. The increase in the total interface energy is $2SWdx$, where S is the surface energy per unit area. Equating the available free energy to the increase in interface energy, one obtains an expression for the interlamellar spacing as a function of the transformation temperature:

$$S_0 = \frac{2T_e S}{\rho Q\,(T_e - T)} \tag{8.2}$$

Thus, the interlamellar spacing is inversely proportional to the degree of undercooling and the heat of formation of pearlite per unit mass, which of course is a function of the composition.

In this regard, recent work was devoted to assess whether a nanostructured pearlite could be obtained by increasing the driving force for pearlite transformation using tailored compositions [271, 272]. Cobalt has been long known to decrease the interlamellar spacing by increasing the driving force for the formation of pearlite [97], and the same effect is observed through aluminum additions [112, 137]. The interlamellar spacing that can be obtained in a eutectoid pearlitic steel with cobalt and aluminum additions by relatively slow continuous cooling at 0.1 °C/s can be as small as 50 nm [271, 272]. It could be speculated that tailored pearlite isothermal transformation at low temperatures would lead to even finer interlamellar spacings.

In general terms, the effect of alloying elements upon pearlite transformation is two-fold: (1) they modify the eutectoid transformation temperature, thereby changing the degree of undercooling at a fixed transformation temperature, and

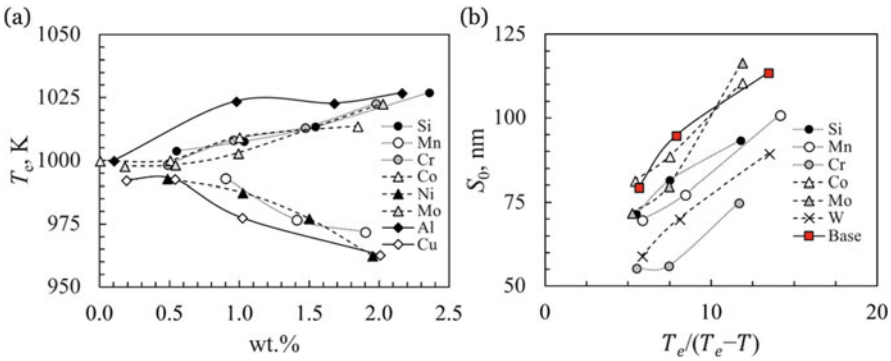

Fig. 8.7 (**a**) Effect of alloying elements on the eutectoid transformation temperature, T_e and (**b**) relationship between the reciprocal of undercooling, $T_e/(T_e - T)$ and interlamellar spacing, S_0, in a 0.8C-0.3Si-0.5Mn (wt.%) steel with different alloying additions of 1 wt.%, except for Mo which is 0.5 wt.%. (Data from [242])

(2) they change the chemical driving force for pearlite formation at a fixed degree of undercooling. For instance, chromium refines the interlamellar spacing at a fixed pearlite transformation temperature by increasing the undercooling, while at the same undercooling, the lamellar spacing is refined by increasing the chemical driving force [104].

Figure 8.7a shows the effect of alloying element additions in a 0.8C-0.3Si-0.5Mn (wt.%) base steel on the eutectoid transformation temperature [242]. It is shown that ferrite stabilizers, silicon, chromium, molybdenum, and aluminum, increase the eutectoid transformation temperature whereas austenite stabilizers, manganese, nickel, and copper, decrease it. At the same time, Figure 8.7b shows the relationship between the reciprocal of undercooling, $T_e/(T_e - T)$ and interlamellar spacing in a 0.8C-0.3Si-0.5Mn (wt.%) steel with 1 wt.% additions of the aforementioned alloying elements (except for Mo, where the addition is of the 0.5 wt.%). In all cases, the interlamellar spacing decreases with the undercooling and reaches values below 100 nm for reciprocal undercoolings below 10, qualifying all these pearlitic structures as nanoscaled. It should be noted that the literature dedicated to basic research on pearlite transformation does not pay much attention to the nanoscaled nature of the structures formed at large undercoolings in alloyed steels, but several examples can be found if the results are carefully examined [104, 137, 193, 261].

Besides, in hypereutectoid pearlitic steels, a detrimental continuous or semi-continuous cementite on the prior austenite grain boundaries may develop during cooling. To avoid this, the steel is alloyed with silicon and vanadium; silicon suppresses grain boundary cementite formation and microadditions of vanadium assists in the suppression process by forming submicron vanadium carbide particles taking the excess carbon from the austenite grain boundary areas [26].

The nanostructure in pearlitic steels is usually achieved at the end of the hot-rolling step by controlled cooling to the desired transformation temperatures. The

heat treating schedule presented in Fig. 8.3 to produce the pearlite structure during patenting can be taken as a reference frame for the production of nanostructured pearlite following large undercoolings. However, forced cooling followed by isothermal treatments is not a common practice in long products, where these steels have their most relevant applicability. Instead, controlled continuous cooling is applied so that transformations occur in a temperature range where the interlamellar spacing is kept to a minimum. Further details will be given in Sect. 5.3.

8.2.3.2 Nanostructured Bainite

As for the case of pearlite, the general trend in bainitic steels is that the plate thickness decreases when the transformation temperature is decreased [220]. The thickness of the bainitic ferrite plates depends primarily on the "strength" of the austenite at the transformation temperature, and the driving force for the transformation, when these variables are treated independently. Strong austenite offers more resistance to interface motion (growth), while a large driving force increases the nucleation rate, both leading to microstructural refinement [46, 220]. The effect of the temperature is implicitly included in both terms, lower temperatures providing austenite strength and increased chemical driving forces. The theory to estimate the bainite and martensite start temperatures, B_S and M_S, respectively [16, 80, 117], was used in the early 2000s to estimate the lowest temperature at which bainite can form.

Figure 8.8a shows the calculated B_S and M_S temperatures whereas Fig. 8.8b shows the time required for bainite transformation to start in a Fe-2Si-3Mn (wt.%) steel as a function of the carbon content [72, 73]. There seems to be no lower limit to the temperature at which bainite can be generated as long as the carbon concentration is increased. In parallel, the rate at which bainite forms slows down

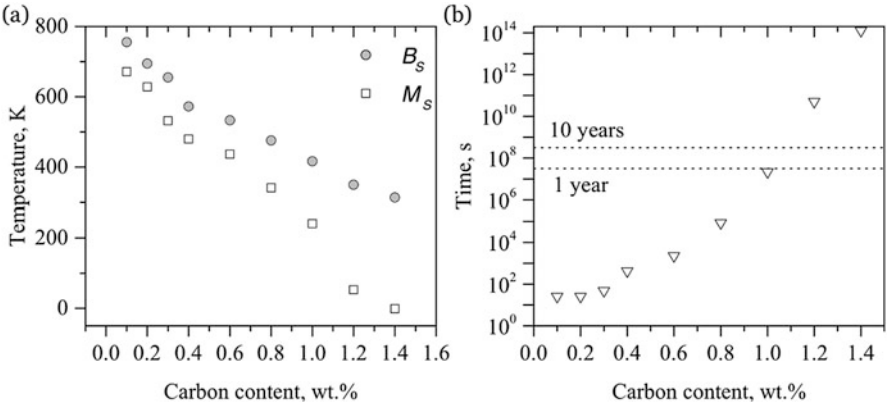

Fig. 8.8 (**a**) Calculated transformation start temperatures in a Fe-2Si-3Mn (wt.%) steel as a function of the carbon concentration, and (**b**) calculated time required to initiate bainite transformation after [72, 73]

exponentially as the transformation temperature is reduced. It may take hundreds or thousands of years to generate bainite at room temperature.[1] For practical purposes, transformation times are nowadays kept up to a maximum of days, corresponding to transformation temperatures between 200 and 350 °C and carbon concentrations from 0.7 to 1.0 wt.% with silicon additions from 1.5 to 3.0 wt.%. The presence of other alloying elements is adjusted to allow hardenability without compromising transformation kinetics. Silicon, as a carbide inhibitor, is added to avoid the precipitation of cementite from austenite during isothermal bainitic transformation. The carbon that is rejected from the bainitic ferrite enriches the residual austenite, thereby stabilizing it (partially or totally) at ambient temperature. However, carbide inhibitors are capable of preventing the precipitation of cementite between the subunits of bainitic ferrite, but they cannot avoid the precipitation of carbides within the ferrite plates in lower bainite [125]. Indeed, during bainite transformation, there are one or more transient intermediate states that have a short lifetime [149, 269], and the relevant precipitation reactions can be best studied in silicon steels since this element retards the precipitation of cementite without influencing the formation of transient carbides [98]. Before nanostructured bainite arose as a metallurgical concept, Sandvik [207, 208] studied the evolution of the bainitic structures formed in high-carbon high-silicon steels transformed at temperatures between 290 and 380 °C, taking advantage of the slow reaction kinetics that permitted a detailed tracking of the different reaction products.

The overall thermodynamics of the diffusionless growth of bainitic ferrite are represented by the T_0 curve, which is the locus of all points on a temperature versus carbon concentration plot, where austenite and ferrite of the same composition have the same free energy, $\Delta G^{\gamma \rightarrow \alpha} = 0$ [16, 282]. In Fig. 8.9a, growth without diffusion can only occur when the free energy of ferrite becomes less than that of austenite of the same composition, i.e., when the concentration of austenite lies to the left of the intersection between the two Gibbs free energy curves. Assuming that a plate of bainitic ferrite forms without diffusion, the excess carbon would afterward be rejected into the surrounding austenite, and the presence of silicon will avoid any precipitation from the carbon-enriched austenite. The next plate then has to grow from carbon-enriched austenite in a process that would stop when the austenite carbon concentration reaches the T_0 curve. This effect is known as the *incomplete reaction phenomenon* [98] since austenite does not reach its equilibrium composition, $x'_{\gamma\alpha}$ given by the Ae'_3 curve, i.e., the $(\alpha + \gamma)/\gamma$ paraequilibrium phase boundary. Considering the stored energy associated with bainite transformation ($\Delta Gs = 400$ J/mol^{-1}) in the Gibbs free energy of ferrite, the condition $\Delta G^{\gamma \rightarrow \alpha} = 0$ is fulfilled at lower carbon content values than in the latter case, as depicted in Figure

[1]To test this theory, two samples of a steel that would take 100 years to transform to bainite at room temperature were manufactured in 2004, one of which can be seen at the Science Museum of London while the other one is stored at Sir Harry Bhadeshia's office in Cambridge University. The samples, sealed in an inert atmosphere, are mirror-polished so that phase changes will be evident through the surface rumples caused by the shear transformation, hopefully in 2104.

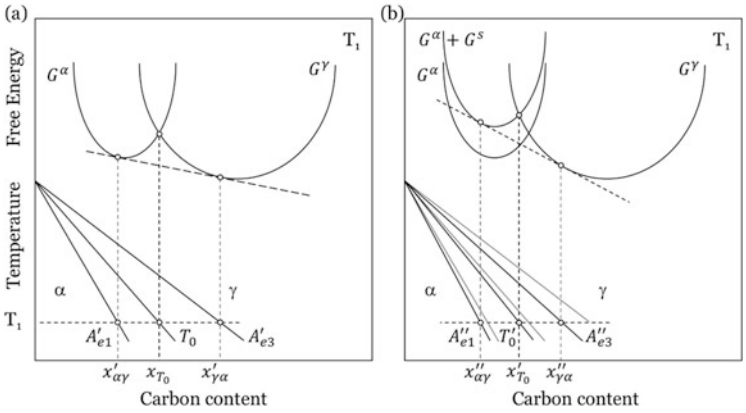

Fig. 8.9 Schematic illustration of the origin of the (**a**) T_0 and (**b**) T'_0 curves on the phase diagram. The T'_0 curve incorporates the strain energy term for ferrite, illustrated on the diagram by raising the free energy curve of ferrite by the term ΔGs. Ae'_1 and Ae'_3 refer to the paraequilibrium phase boundaries $\alpha/(\alpha + \gamma)$ and $(\alpha + \gamma)/\gamma$, respectively. Ae''_1 and Ae''_3 are the corresponding phase boundaries allowing for the stored energy

8.9b. Thus, the T'_0 and Ae''_3 curves are obtained when the T_0 and Ae'_3 curves are modified to account for the stored energy of transformation, respectively [20]. Under these circumstances, the process will cease when the austenite carbon concentration reaches the T'_0 curve (x'_{T_0}).

Therefore, nanostructured bainite, also termed nanobainite, superbainite, or low-temperature bainite, is the reaction product of the austenite obtained in high-carbon, high-silicon steels after isothermal transformation at temperatures below 350 °C. It is a form of lower bainite consisting of a mixture of bainitic ferrite plates with nanoscale precipitates and retained austenite. In practice, the nanostructures are obtained outside a continuous production line through proper heat treating, usually requiring the use of salt baths, with the exception of smaller dimensions components amenable to dry heat treatments. The temperature control during the isothermal step is key to obtain the structures, given that transformation times grow exponentially with decreasing the transformation temperature. Deviations from the target temperature to lower temperatures may lead to too short times available for the steel to be fully bainitic, with large portions of detrimental untransformed retained austenite. The block morphology of untransformed austenite is deleterious to toughness when it transforms into martensite at an early stage of deformation.

8.3 Microstructure Description at the Multiscale

8.3.1 Nanostructures in Steels Produced by Wire Drawing

The carbon content in cold-drawn pearlitic steel wires is in the range of 0.75 and 1.00 wt.%, with small additions of other alloying elements, and little or no addition of carbide formers, i.e., they are fully pearlitic after proper patenting treatment. The initial material usually consists of a patented wire with a diameter of 1.70 mm, as described in [241]. Figure 8.10 shows the cross-section microstructure of a 0.82 wt.% C patented steel wire [103]. Figure 8.10a presents a bright-field transmission electron microscope (TEM) image containing two micron-sized pearlite colonies, with a uniform interlamellar spacing within each colony (about 130 nm). The bright-field TEM micrograph in Fig. 8.10b was taken from the cementite reflection encircled in Fig. 8.10a and shows planar defects (indicated by arrows) that can be attributed to stacking faults or slip traces resulting from internal strain [110, 214]. Both the patenting temperature and the composition of the steel have a remarkable effect on the interlamellar spacing, the interlamellar spacing decreasing with the increase in the carbon composition of the steel and the decrease in the patenting temperature [171, 248].

Successive cold drawing reduces the width of both ferrite and cementite lamellae due to increasing strain and also aligns the originally randomly oriented lamellae belonging to different colonies parallel to the wire axis. In pearlite wires, the microstructural architecture is not changed during moderate deformations, but soaring strains cause morphological changes, namely fiber curling [105, 238, 241]. Figure 8.11 presents the cross-section microstructure of a 0.82 wt.% C patented steel wire drawn to a true strain of 4.22 [103]. Figure 8.11a shows a bright-field TEM micrograph where the pearlite lamellae exhibit bending around the wire axis

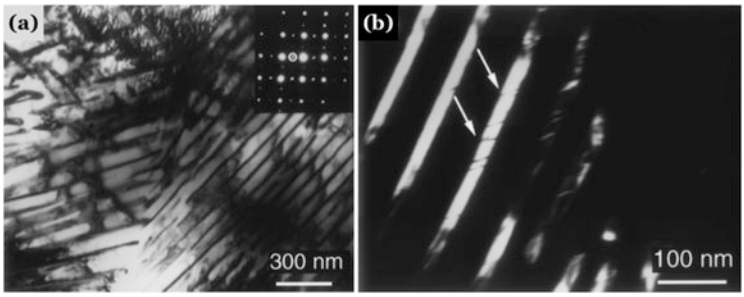

Fig. 8.10 Cross-sectional (**a**) bright-field and (**b**) dark-field TEM images of patented 0.82C-0.5Mn-0.25Si (wt.%) pearlitic steel wire. The beam direction is close to the [001] zone of ferrite. The image in (**b**) was obtained using the cementite reflection circled in (**a**). Reprinted by permission from Springer Nature: Springer Metals and Materials Transactions A, Atom Probe and Transmission Electron Microscopy Investigations of Heavily Drawn Pearlitic Steel Wire, Hong et al. [103]

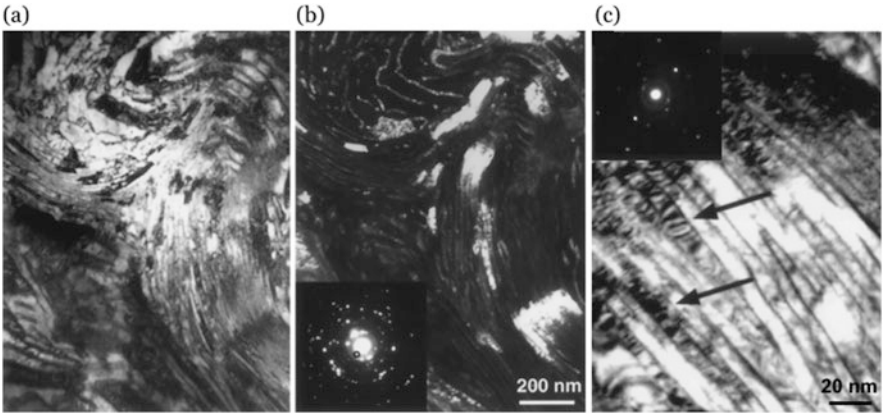

Fig. 8.11 Cross-sectional TEM images of a 0.82C-0.5Mn-0.25Si (wt.%) pearlitic steel wire drawn to a true strain of 4.22 (**a**) bright field and (**b**) corresponding dark field where the cementite reflection used is encircled in the selected-area diffraction pattern (inset), and (**c**) bright-field image showing the contrast arising from regions of local strain (arrowed) found throughout the ferrite lamellae. Reprinted by permission from Springer Nature: Springer Metals and Materials Transactions A, Atom Probe and Transmission Electron Microscopy Investigations of Heavily Drawn Pearlitic Steel Wire, Hong et al. [103]

with a curled structure, tending to fragment into a ribbon-like morphology. The interlamellar spacing varies significantly from one ferrite to another, and it appears that adjacent ferrite ribbons have different orientations, given the darker or lighter contrast of the ferrite. Figure 8.11b shows a dark-field TEM micrograph taken from the cementite reflection of the inset. After heavy straining, cementite lamellae are fragmented into small grains, and individual dislocations, as shown in Fig. 8.10b, are no longer resolvable. The bright-field TEM micrograph in Fig. 8.11b reveals strain contrast throughout the ferrite lamellae, which is thought to arise from highly-dislocated regions. Furthermore, selected-area diffraction patterns in the insets of Fig. 8.11b and c include both ferrite reflections and rings corresponding to cementite interplanar spacings, the latter resulting from randomly oriented fragmented cementite grains, not revealed in the dark-field in Fig. 8.11b.

Figure 8.12 shows three-dimensional carbon atom maps of a 0.98C-0.31Mn-0.20Si-0.20Cr (wt.%) pearlitic steel wire in longitudinal (left) and cross-sectional (right) views relative to the drawing direction in samples drawn to low (1.96), medium (4.19), and extremely high strains (6.52) [136]. The 7 at.% C green isosurfaces are drawn to separate the carbon-enriched regions identified as cementite from the carbon-depleted ferrite regions. At low drawing strains, the lamellae align in parallel to the drawing directions without a significant change in the morphology but with certain fragmentation of the cementite lamellae. As the drawing strain increases, the volume fraction of cementite continuously decreases by mechanically driven chemical decomposition thereby releasing carbon into the ferrite matrix, which gets carbon-supersaturated [79, 94, 110, 111, 130, 157, 211, 214]. Successive

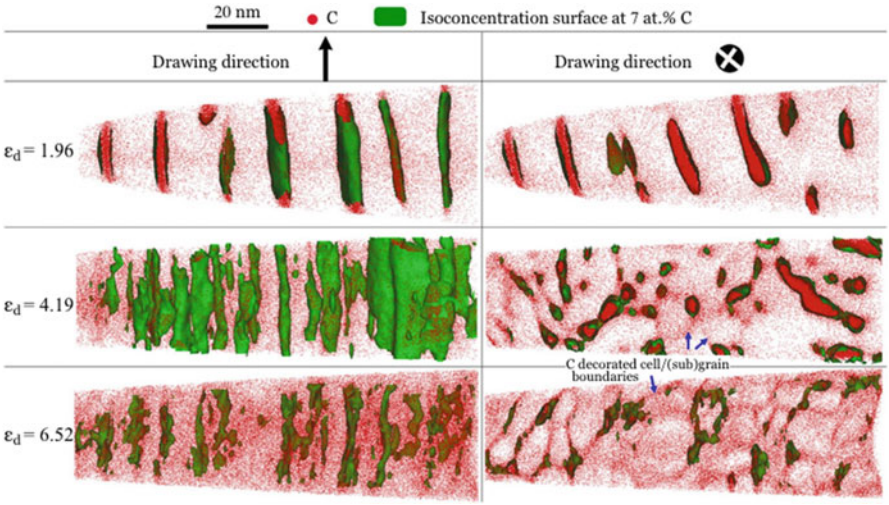

Fig. 8.12 Three-dimensional carbon atom maps with the 7 at.% C isosurfaces superimposed in both longitudinal (parallel to the drawing direction, left) and cross-section (perpendicular to the drawing direction, right) of a 0.98C-0.31Mn-0.20Si-0.20Cr (wt.%) pearlitic steel wire cold drawn to different drawing strains. Blue arrows indicate some of the subgrain boundaries decorated with carbon atoms. ε_d is the true drawing strain. Reprinted by permission from American Physics Society: American Physics Society and Physical Review Letters, Segregation Stabilizes Nanocrystalline Bulk Steel with Near Theoretical Strength, Li et al. [136]

cold-drawing results in a reduction of the cementite volume fraction to values of about 6 vol.% or less, with a concomitant decrease of its carbon content from 25 at.% (6.67 wt.%) to values around 12.5 at.% (3.0 wt.%), depending on the thickness of the individual lamellae [23]. At extremely high strains, the lamellar structure evolves into a nearly equiaxed ferrite subgrain structure with carbon atoms segregating at the boundaries (indicated by the blue arrows).

The stability of the nanoscaled multiphase structure can be easily tested by annealing treatments at different temperatures. Figure 8.13 shows the effect of various annealing treatments on the microstructure of a 0.82C-0.5Mn-0.25Si (wt.%) pearlitic steel wire drawn to a true strain of 4.22 in longitudinal view [103]. The microstructure of the as-drawn wire in Fig. 8.13a shows little or no difference with the microstructure after annealing at 200 °C for 1 h in Fig. 8.13b. Indeed, the strain contrast in ferrite remains after annealing at 200 °C, while the cementite preserves the fragmented nanocrystalline structure. Annealing at higher temperatures leads to significant microstructural changes. After annealing at 400 °C for 1 h (Fig. 8.13c), the interlamellar spacing is coarser than in the as-drawn state, and cementite grains of about 30 nm and above are observed all throughout the microstructure, even within the ferrite lamellae. The lamellar structure is lost after annealing at 500 °C for 1 h, originated by spheroidization of cementite and recovery and recrystallization of ferrite, as Fig. 8.13d illustrates. In general, there are no substantial changes in the

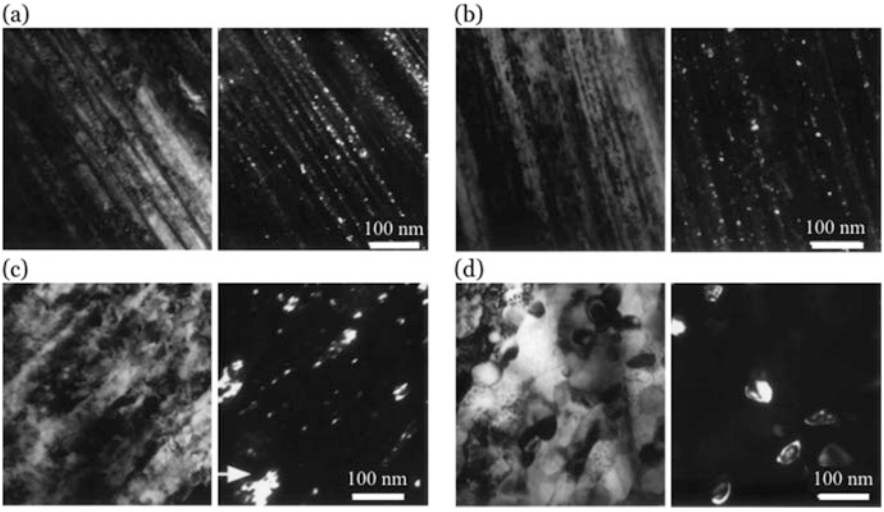

Fig. 8.13 The effect of annealing on the microstructure of a 0.82C-0.5Mn-0.25Si pearlitic steel wire drawn to a true strain of 4.22. Bright-field/dark-field TEM image pairs are taken perpendicular to the wire axis (longitudinal view): (**a**) as-drawn wire; (**b**) annealed at 200 °C for 1 h; (**c**) annealed at 400 °C for 1 h; and (**d**) annealed at 500 °C for 1 h. Reprinted by permission from Springer Nature: Springer Metals and Materials Transactions A, Atom Probe and Transmission Electron Microscopy Investigations of Heavily Drawn Pearlitic Steel Wire, Hong et al. [103]

nanostructures after annealing at temperatures below 250 °C, whereas annealing at higher temperatures results in time-dependent spheroidization of both ferrite and cementite lamellae [23, 101, 103, 135, 156, 182, 239].

8.3.2 Nanostructures in Steels Produced by Mechanical Alloying

8.3.2.1 Structure of the Matrix in NFAs

Immediately after the mechanical alloying process, the powders have a grain size that can be as fine as 1–2 nm locally [113]. This is a consequence of the extent of the deformation during mechanical alloying, with true strains of the order of 9, equivalent to stretching a unit length by a factor of 8000. The consolidation process involves hot extrusion and rolling at temperatures of about 1000 °C, which leads to microstructure of as-extruded NFAs consisting on elongated grains along the extrusion direction with a high grain aspect ratio.

Figure 8.14 shows the grain structure in a 14 wt.% Cr ODS steel hot extruded into bars at 1100 °C, in both the longitudinal and transverse directions [39]. The grain structure in the longitudinal direction is composed of large elongated grains,

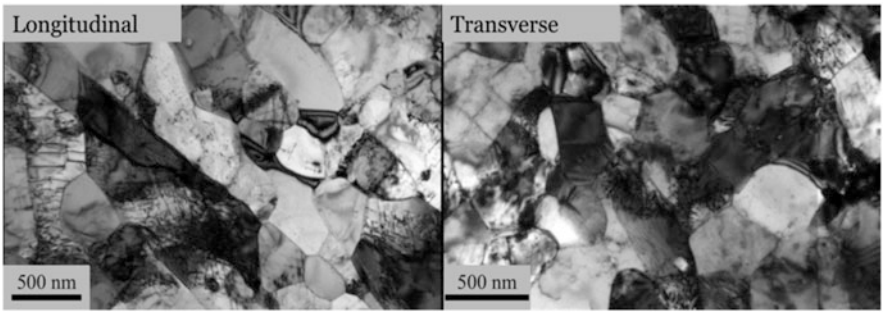

Fig. 8.14 TEM bright-field micrographs from as-received ODS Fe-14 wt.% Cr steel (ferritic). (**a**) Longitudinal direction revealing elongated as well as equiaxed grains. (**b**) Transverse direction revealing small equiaxed grains. In both directions, regions with different dislocation density are apparent. Reprinted with permission from Elsevier: Journal of Nuclear Materials, Microstructure characterization and strengthening mechanisms of oxide dispersion strengthened (ODS) 9 wt.% Cr and 14 wt.% Cr extruded bars, Chauhan et al. [39]

together with regions of small equiaxed grains, while in the transverse direction the grains are smaller and equiaxed. The average dislocation density is about 5×10^{14} m^{-2}, with the presence of regions with different dislocation density.

The typical grain size in NFAs is below 300 nm, usually showing a bimodal distribution of the grain size in different regions of the transverse direction. This bimodal grain structure is also observed in conventional ODS alloys and is likely to be due to differences in the amount of milling locally imparted during mechanical alloying and the resulting grain refinement [39, 154, 155, 174].

It is known that during the course of consolidation, the material may dynamically recrystallize several times [35, 36, 93]. It should be emphasized that the submicron grains are not low-misorientation cell structures, but true grains with large relative misorientations [17].

The resulting crystallographic texture in ODS steels and NFAs is a consequence of the manufacturing route [8, 38, 54, 145, 179]. For instance, the PM2000 alloy supplied in the form of a hot-rolled tube (finish rolling temperature of ~1050 °C) of 100 mm diameter and 7.9 mm thickness air cooled to room temperature shows an incomplete α-fiber texture (RD‖<110>) with a dominant {001}<110> component, i.e., the {100} crystallographic planes parallel to the tube surface and the <110> crystallographic directions parallel to the rolling direction. On the other hand, the MA956 alloy having a similar composition to that of the PM2000 alloy, but supplied in the form of a hot-extruded bar (extrusion temperature of ~1050 °C) of 60 mm diameter air cooled to room temperature, presents an α-fiber (ED‖ < 110>) texture with a strong {111}<100 > γ-fiber component. Figure 8.15a and b show the orientation distribution function (ODF) at $\varphi_2 = 45°$ for as-hot-rolled PM2000 alloy and as-hot-extruded MA956 alloy, respectively. To ease the interpretation, Fig. 8.15c shows the ODF section with $\varphi_2 = 45°$ indicating the position of the major components of texture in ODS steels.

Upon subsequent cold-rolling of ODS steels and NFAs, the crystallographic texture produced consists of both α-fiber components such as {001}<110> and

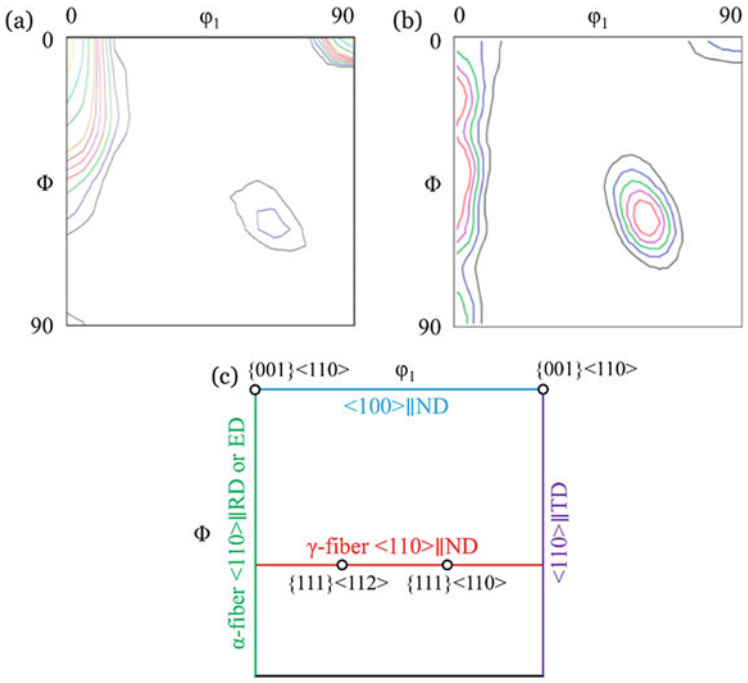

Fig. 8.15 Orientation distribution function (ODF) at $\varphi_2 = 45°$ for (**a**) as-hot-rolled PM2000 alloy, (**b**) as-hot-extruded MA956 alloy, and (**c**) the major components of texture in ODS steels. (Adapted from [38])

{112}<110> and γ-fiber components such as {111}<110> and {111}<112> [9, 132, 133, 216], depending on the cold rolling direction relative to the original hot-rolling or -extruding direction. In this sense, investigations on cold-rolling processes have been intended to change the original texture after fabrication and its effect upon recrystallization.

8.3.2.2 Structure of the Oxides in NFAs

During intensive milling of the system, the powder particles get work-hardened and their grain structures are refined. At the same time, yttrium and titanium atoms are forced into the matrix, either forming solid solution or amorphous sub-nanometric fragments [100]. The lattice distortions are intensified by the addition of large solute elements (yttrium, titanium) at substitutional positions and oxygen atoms at interstitial sites, which can promote the build-up of a large dislocation density by reducing the level of dynamic recovery. Since the solubility of both titanium and yttrium in alpha iron is low, the driving force for the precipitation of titanium and yttrium oxides in the matrix is very high. Precipitation being a

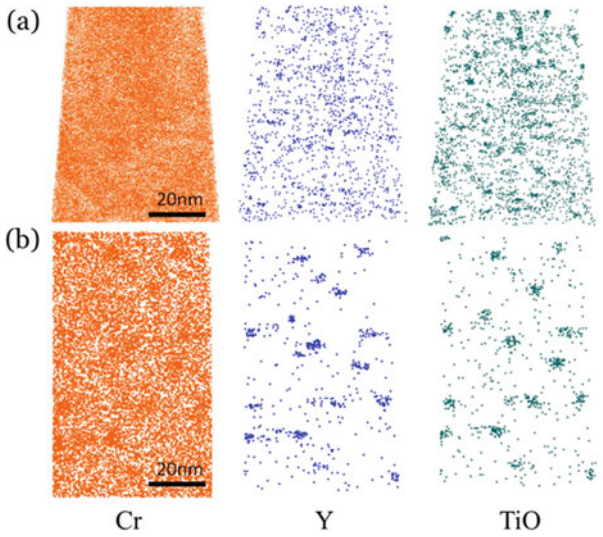

Fig. 8.16 Five-nanometer-thick slice of an atom map showing the distribution of Cr, Y, and Ti-O ions in a 14Cr–2 W–0.3Ti–0.3Y_2O_3 (nominal, wt.%) ferritic steel (**a**) powder immediately after MA and (**b**) after degassing; HIP consolidation at 1150 °C for 4 h and further annealing at 1150 °C for 100 h. Reprinted with permission from Elsevier: Acta Materialia, The formation and evolution of oxide particles in oxide-dispersion-strengthened ferritic steels during processing, Williams et al. [268]

diffusion-activated mechanism, it is assumed that they form only during the high-temperature consolidation process [24]. Yttrium is added under the form of yttrium oxides (Y_2O_3), and the oxygen content is, therefore, directly related to the content of these oxides. In addition to this direct oxygen source, there is a second oxygen source referred to as "excess oxygen" resulting from contamination during milling, although the oxygen quantity brought by this second source is far from negligible [268].

Clustering of yttrium and titanium is observed in the powder after a certain milling time [268], as shown in Fig. 8.16a. Perfect solid solution with a random distribution of solute atoms is difficult to achieve, especially for elements with low solubility in bcc iron. However, there is general agreement with the fact that these sub-nanometric clusters are homogeneously distributed in the powder. Also, after annealing or consolidation at high temperature, the clusters tend to crystallize and form nano-oxide precipitates [271, 272]. The number densities and volume fractions of the nano-oxides decrease and their radii increase with increasing consolidation temperature [2].

The importance of dissolved titanium relies on the refinement of the Y_2O_3 precipitates [250] due to the reactions leading to the formation of complex oxides having typical sizes of a few nanometers [175, 251, 275]. The stoichiometry and crystal structure of the oxide nanoparticles have been long debated, partly due to

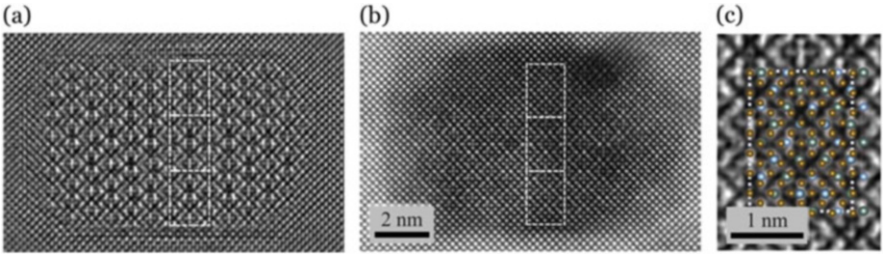

Fig. 8.17 (**a**) Phase of the reconstructed exit wave from focal series (under, near, and over focus) in a high-resolution TEM image of a large nano-oxide, (**b**) corresponding high-angle annular dark-field (HAADF) scanning transmission electron microscope (STEM) image where the dashed lines highlight the periodicity of the Moiré pattern in the overlap region, (**c**) magnified views of the periodic structure in the exit-wave reconstruction image. The dashed lines show the periodic repeated pattern of 5 × 7 Fe unit cells, while the colored balls represent lateral positions of Y (green) and Ti (blue) columns relative to the Fe (yellow) matrix. Reprinted with permission from Elsevier: Acta Materialia, The crystal structure, orientation relationships and interfaces of the nanoscale oxides in nanostructured ferritic alloys, Wu et al. [273]

the use of different techniques, each of them having different limitations: XRD, TEM, atom probe tomography (APT), and small-angle neutron and X-ray scattering (SANS and SAXS) [173, 175]. Nowadays, there is general agreement that the smallest cubic and cuboidal oxide nanoparticles are the face-centered cubic (fcc) $Y_2Ti_2O_7$ pyrochlore phase [174], while larger oxides in NFAs are observed to be Y_2TiO_5 oxides [271, 272]. As an example, Figure 8.17a and b show a periodic image pattern in the central region of a small nano-oxide, reflecting the overlap the $Y_2Ti_2O_7$ pyrochlore and the ferrite matrix crystal structures formed in the MA957 NFA. Figure 8.17c shows the corresponding overlays of an ideal $Y_2Ti_2O_7$ pyrochlore atomic model with the observed orientation relationship. The dashed lines correspond to a periodic array of 5 × 7 Fe periodic cells, while the colored balls represent lateral positions of Y (green) and Ti (blue) atoms relative to the Fe matrix (yellow), based on a visual best fit position adjustment of the image intensities [273]. Thus, the smallest nano-oxides have a coherent cube-on-edge interface, where the oxides are under compressive stress while the matrix is under tension [273]. The interface of larger oxides is semicoherent [274], with misfit dislocation structures in the ferrite matrix. At the same time, there is evidence of oxide nanoparticles exhibiting core-shell structures with oxygen, chromium and/or titanium enrichments at the interface [140]. The relevance of the oxide-ferrite interface in NFAs relies on its ability to trap helium.

Besides, the $Y_2Ti_2O_7$ have a remarkable thermal stability, remaining essentially stable for thousands of hours at temperatures below 900 °C [50, 175]. Such stability derives from the low solubility of yttrium in local equilibrium with $Y_2Ti_2O_7$ [50]. At higher temperatures, the coarsening mechanism is pipe diffusion along dislocations, where the yttrium is more soluble than in the matrix and migrates more rapidly. In parallel, grain sizes and dislocation densities are stable at the same temperatures, at least for some tens of thousands of hours [49, 50].

8.3.2.3 Recrystallization Behavior of NFAs

Recrystallization in ODS steels occurs at exceptionally high homologous temperatures, of the order of 0.9 of the melting temperature (T_M in Kelvin). This contrasts with ordinary cold-deformed metals that recrystallize readily at about 0.6 T_M. The reason for such intriguing behavior remains unclear; some authors have speculated [114] that recrystallization occurs when the grain boundaries overcome solute drag and the mobility rises suddenly at high temperatures. This is inconsistent with some experimental evidences that demonstrate that the recrystallization temperature can be reduced by many hundreds of Kelvin by a slight additional inhomogeneous deformation [41, 133, 195]. Conversely, other authors suggested that the fine particles of yttrium oxide may offer a hard pinning for moving boundaries during recrystallization but this does not explain the reason for the enormous limiting grain size following recrystallization. In any case, recrystallization is found to be insensitive to the overall pinning force [165].

The recrystallization process of ODS steels and NFAs consists of two well-defined stages: extended recovery and abnormal grain growth [24, 189]. During the whole recrystallization process the submicron elongated grains along the rolling direction in the as-rolled microstructure evolve to assemble a coarse microstructure with the millimeter-sized grains presenting a preferential <112> orientation parallel to the rolling direction. At the first stage, the alloy undergoes an extended recovery process characterized by a geometrical change in the grain morphology from an elongated to an equiaxed structure. Here, new grains are not nucleated, and no significant change in material texture is observed [189], although there is a strengthening in the texture component towards the (001)<110> (lower Taylor factor) due to grain rotation driven by dislocation glide.

The uniform microstructure with the α-fiber texture component prior to coarse grain microstructure is strengthened by the increase of low-angle grain boundaries (LAGBs) due to subgrain rotation driven by dislocation glide. This promotes the orientation pinning mechanism of high-angle grain boundaries (HAGBs), which require an enormous energy to unpin the grain boundaries. This fact explains the reason for recrystallization (generation of coarse grained microstructure) requiring elevated temperatures of 0.9 of the absolute melting temperature. The orientation pinning term was used for the first time by Juul Jensen et al. [115] to describe the fact that the grain boundary mobility depends on the orientation relationship between the growing grains and the surrounding matrix material. If the growing grain is separated from the matrix by a HAGB, and the misorientation between this grain and the matrix is reduced because of the grain rotation, the HAGB evolves to a LAGB which presents a substantially reduced mobility. Therefore, the growth of the grain is stopped after a certain time. This is consistent with the increasing number density of LAGBs with annealing time detected during the recrystallization of PM2000 [35]. Besides, the increased number of LAGBs is also responsible for the pinning of the HAGBs between grains with a strong texture [115].

In this context, weak texture grains of <112> present a substantially higher mobility than those of the matrix with strong texture (RD || <110>). Therefore,

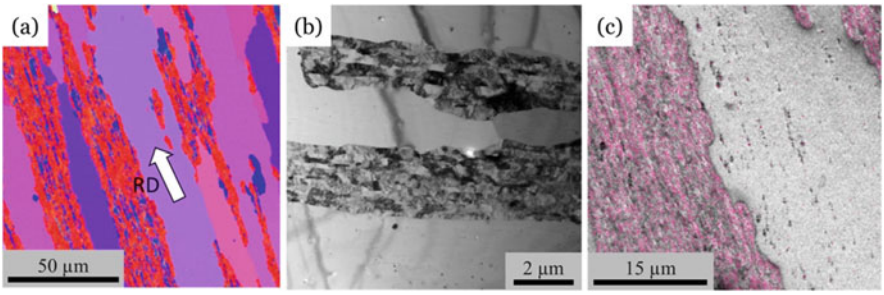

Fig. 8.18 Microstructure of the 14YWT NFA after 60% compression and further annealing at 1100 °C for 7.5 h showing recrystallized, abnormally grown, and unrecrystallized regions. (**a**) Electron backscatter diffraction (EBSD) orientation distribution (inverse pole figure) map, where the arrow indicates the rolling direction (RD) perpendicular to the compression direction and the low-angle grain boundaries having misorientation of 0.5°–2°are the red lines, (**b**) bright-field TEM image, and (**c**) EBSD band contrast gray scale map showing the low-angle grain boundaries having misorientation of 0.5°–2° (pink lines) in abnormally grown and recovered and unrecrystallized grains. Reprinted with permission from Elsevier: Acta Materialia, High temperature microstructural stability and recrystallization mechanisms in 14YWT alloys, Aydogan et al. [9]

the <112> oriented grains, present in the as-hot-rolled microstructure with their associated relatively high-mobility HAGBs, provide the seeds for the nucleation of abnormal grain growth in the second stage of the recrystallization process.

Figure 8.18 illustrates the structure of the 14YWT NFA after 60% compression and further annealing at 1100 °C for 7.5 h, where recrystallized, abnormally grown (size >50 μm), and unrecrystallized/recovered regions coexist, with no texture change in the latter regions [9]. These results corroborate that in NFAs, abnormal grain growth occurs with no incubation time, and recrystallization and abnormal grain growth occur simultaneously above 850 °C [206].

As aforementioned, the increase of misorientation between neighboring grains due to cold deformation weakens the orientation pinning, triggering the recrystallization [9, 132, 133, 216]. When NFA products require cold rolling after hot extrusion, such as in clad tubes,[2] recrystallization control is essential to obtain the required strength and ductility in the hoop direction. Here, thermomechanical processing aims to produce unrecrystallized cold-rolled forms at an intermediate process followed by a recrystallization only at final heat treatment [168]. Recrystallization in NFAs after cold deformation remains a key issue particular to each case study. In general terms, the temperature of the onset of recovery and recrystallization is closely related with deformation texture and dissolution-reprecipitation mechanisms of the nano-oxides [9, 132, 133, 216].

[2]Claddings are tubes with an outer diameter of ~10 mm and a wall thickness of 1 mm. Seamless tubes are produced according to well-established procedures leading to a pronounced texture after heat treatment.

The improved high-temperature strength of NFAs is the result of the effect of oxide nanoparticles in pinning movable dislocations and inhibiting grain growth at elevated temperatures. During the extended recovery stage, particles play a crucial role in suppressing grain boundary mobility by the well-known Zener pinning effect. The presence of nanoscale oxide particles in the microstructure may exert an anisotropic pinning force on grain boundaries, and this explain the differences between transverse and longitudinal grain boundary velocities reported by Capdevila et al. [36]. Nevertheless, the equiaxed grain morphology during the extended recovery stage is closely related to the coarsening of the oxides located at the grain boundaries. After the extended recovery stage, the grain growth is only suppressed by the orientation pinning mechanism described previously [189]. Only those grains which are not likely to undergo orientation pinning will evolve to form the recrystallized coarse grained microstructure characteristic of this class of material.

The coarsening rate of the oxide particles and their link to recrystallization of the matrix are altered as a function of the annealing temperature and differ from one alloy to another [216]. As an example, unrecrystallized grains in Fig. 8.18b have particles with a large aspect ratio while the nanoparticles in the recrystallized and abnormally grown grains are round and coarser. This is explained on the basis of a dissolution-reprecipitation process of the nanoparticles [206]. It is speculated that elongated and undissolved particles in the unrecrystallized areas pin the dislocations during annealing, while dissolution and reprecipitation of nano-oxides occur on the dislocation boundaries along the deformation direction. As a consequence, particles aligned in the deformation direction prevent recrystallization (Fig. 8.18b), whereas in the regions lacking these particles, after deformation, undergo recovery before reprecipitation occurs (Fig. 8.18c).

8.3.3 Nanostructures in Steels Produced by Solid Reaction

8.3.3.1 Nanostructured Pearlite

The basic structure of pearlite has been introduced in Sect. 3.1 for patented wires and is not repeated here for the sake of brevity. Figure 8.19 shows TEM images of nanostructured pearlite produced in a hypereutectoid steel containing vanadium microadditions. Two pearlite nodules are observed, where the Moiré fringes between the ferrite and cementite lamellae indicate that the structure is not parallelly aligned with the beam, and thus the interlamellar spacing here measured is greater than the true spacing. The dark-field image in Fig. 8.19 reveals a uniform distribution of tiny vanadium carbides within the ferrite lamellae.

Measurements of the interlamellar spacing of pearlite can be conducted in a simple manner by using properly prepared and etched metallographic specimens using circular test grids to determine the mean random spacing using either scanning electron microscopy (SEM) replicas or SEM images. A number of randomly chosen

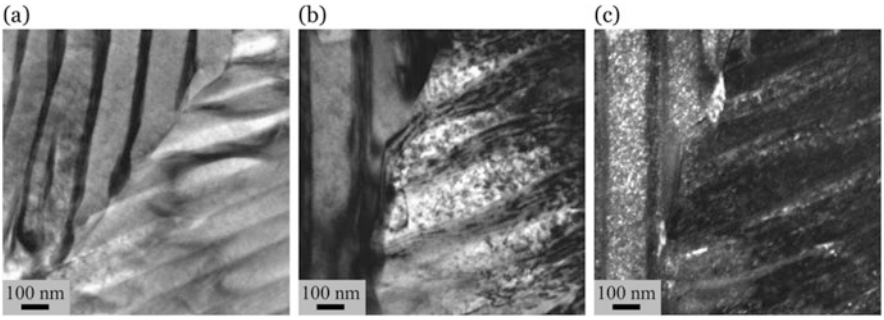

Fig. 8.19 TEM images of pearlite produced in a hypereutectoid steel micro-alloyed with vanadium. (**a**) Bright-field image of ferrite and cementite in two pearlite nodules, (**b**) bright-field image of vanadium carbides in interlamellar ferrite, and (**c**) dark-field image of vanadium carbides in ferrite locations of the left nodule (ArcelorMittal Global R&D internal report)

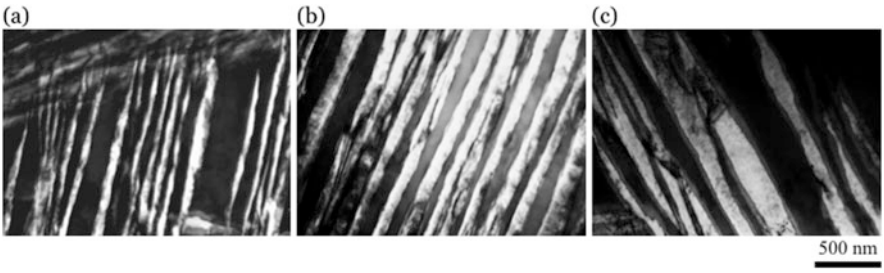

Fig. 8.20 Bright-field TEM images of the structures formed in a 0.98C-1.46Si-1.89Mn-0.26Mo-1.26Cr-0.09 V (wt.%) steel isothermally transformed at (**a**) 200 °C for 15 days, (**b**) 250 °C for 30 h and, (**c**) 300 °C for 9 h. (Authors' own unpublished work)

fields should be measured to obtain adequate statistics, and the mean true spacing is calculated as half the mean random spacing [253], meaning that direct rough estimations without stereological correction are overestimated. Directed spacing measurements in TEM thin foils by tilting the specimen take much more effort, and the correlation between the directed spacing measurement and the true interlamellar spacing is empirical in nature [256, 257]. The interlamellar spacing in the steel shown in Fig. 8.19 measured using SEM micrographs is about 85 nm.

8.3.3.2 Nanostructured Bainite

Figure 8.20 presents bright-field TEM images of the structures obtained in a 0.98C-1.46Si-1.89Mn-0.26Mo-1.26Cr-0.09 V (wt.%) steel isothermally transformed at temperatures between 200 and 300 °C. The bright contrast corresponds to the bainitic ferrite plates, while the dark contrast corresponds to retained austenite

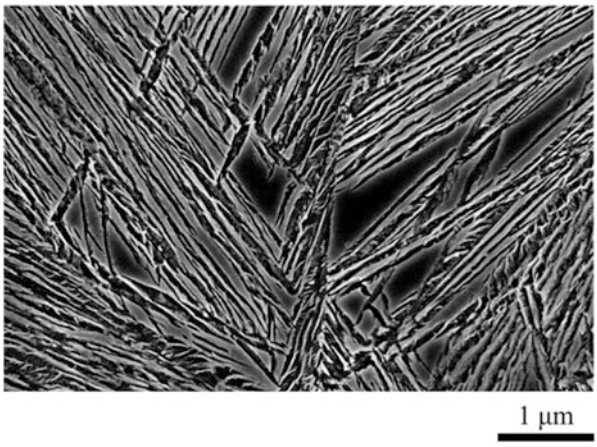

Fig. 8.21 SEM micrograph of a 1.0C-1.47Si-0.74Mn-0.97Cr (wt.%) steel after incomplete transformation at 200 °C for 22 h showing large blocks of retained austenite in between bainite sheaves formed at a prior austenite grain boundary and thin films between bainitic ferrite plates within the sheaves. Lower relief etched regions correspond to bainitic ferrite, while upper relief regions are retained austenite. (Authors' own unpublished work)

regions. It is easy to note that the scale of the bainitic ferrite plates is refined when decreasing the transformation temperature. After stereological correction [143], the thickness of the ferrite plates is determined to be of about 35 nm for the steel isothermally transformed at 200 °C (Fig. 8.20a), 55 nm for transformation at 250 °C (Fig. 8.20b), and 125 nm for transformation at 300 °C (Fig. 8.20c) [72, 73]. Thus, nanostructured bainite mainly consists of bainitic ferrite plates embedded in a network of retained austenite.

Retained austenite presents two distinguishable morphologies, i.e., thin films between platelets of bainitic ferrite and blocks between sheaves of bainite, as presented in Fig. 8.21. The carbon content distribution in the austenite goes hand in hand with the austenitic feature size distribution, thin films being more enriched in carbon than blocks [31, 75, 199, 200]. Austenite transformation into bainitic ferrite is regarded as a division process, where ferrite plates divide the austenite into films, and the sheaves (or aggregates of plates) divide the austenite into blocks. In the early stages of bainite transformation in silicon-containing steels there are two populations of austenite: one having a higher carbon content in the surrounding of the ferrite plates and the other, having a carbon content close to nominal in areas far from the ferrite [247]. As the transformation progresses, with the subsequent carbon partitioning from the ferrite towards the austenite, the austenite blocks diminish in scale getting enriched in carbon and evolving into films as bainitic ferrite plates breach them. The carbon content of the retained austenite after transformation is complete is slightly above the value given by the T_0' curve.

Figure 8.22a exemplifies an APT needle obtained from a 0.66C-1.45Si-1.35Mn-1.02Cr (wt.%) steel transformed at 220 °C for 168 h, where carbon isoconcentration

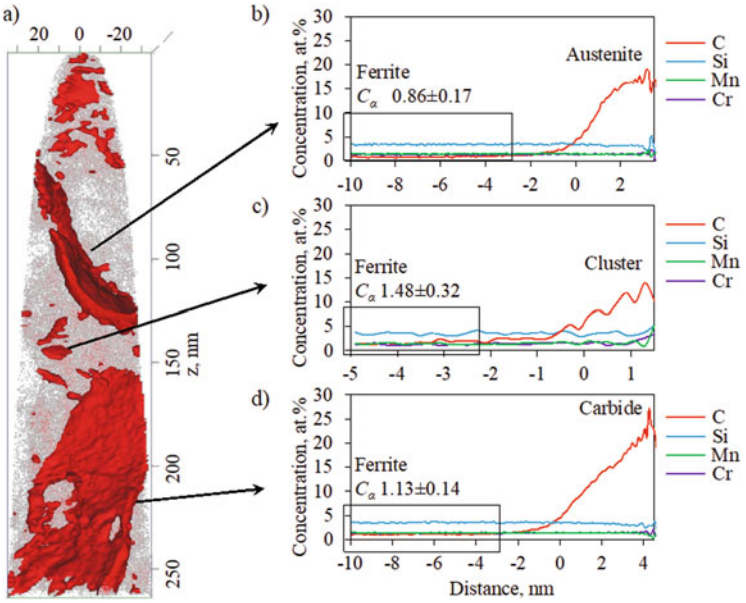

Fig. 8.22 APT measurements on a 0.66C-1.45Si-1.35Mn-1.02Cr (wt.%) steel transformed at 220 °C for 168 h showing carbon isoconcentration surfaces at 6 at.% superimposed with the carbon atom map and proximity histograms across the interfaces indicated by arrows which correspond to (**a**) ferrite/austenite interface, (**b**) ferrite/cluster interface, and (**c**) ferrite/carbide interface. (Authors' own unpublished work)

surfaces at 6 at.% C are superimposed with the carbon atom map. As no crystallographic information is available through this technique, the low carbon regions are usually assumed to be the ferrite phase, while high carbon regions are identified according to their carbon content and morphology [32, 246]. Figure 8.22b, c and d show the proximity histograms obtained across a ferrite/austenite interface, a carbon cluster, and a ferrite/carbide interface, respectively. As here observed, nanostructured bainitic ferrite exhibits a complex nonhomogeneous distribution of carbon atoms in arrangements with a specific composition, a few nanometers in size in most cases. These carbon-enriched regions are identified from their carbon content as Cottrell atmospheres (~8 at.% C), carbon clusters (~11 at.% C), the $Fe_{32}C_4$ carbide (20 at.% C), and cementite or η-carbide precipitates (25 at.% C) [32, 33, 186, 199, 200, 246].

Besides, APT observations show that large amounts of excess carbon remain in the baintic ferrite matrix [30, 199, 200, 246], justified by a body-centered tetragonal, rather than body-centered cubic, symmetry of the ferrite lattice [77, 108, 247]. It is suggested that the tetragonality detected would be the result of carbon clusters, with a locally increased tetragonality, surrounded by a depleted matrix [199, 200], which is representative of the early stages of decomposition of ferrous martensites [244]. The reasons for such carbon-supersaturation still remain a matter of discussion

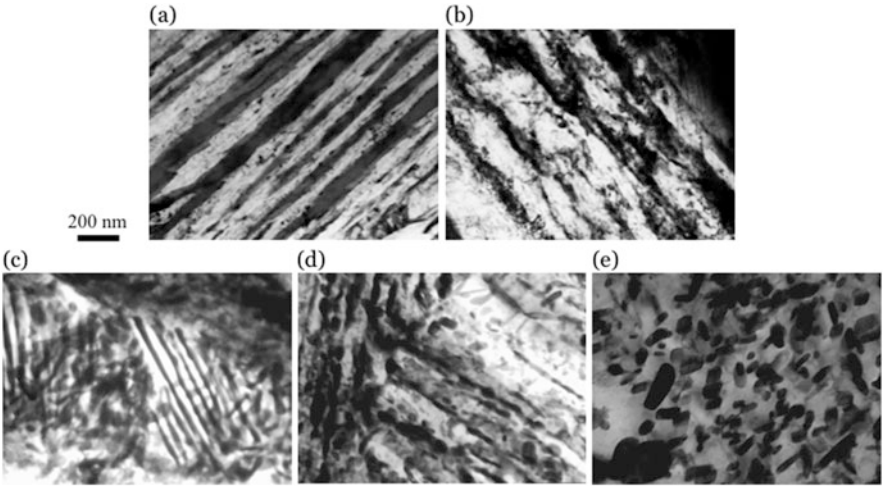

Fig. 8.23 Bright-field TEM images of a 0.98C-1.46Si-1.89Mn-0.26Mo-1.26Cr-0.09V (wt.%) steel isothermally transformed at 200 °C for 45 days and tempered at (**a**) 400 °C for 1 h, (**b**) 450 °C for 1 h, (**c**) 550 °C for 1 h, (**d**) 600 °C for 30 min, and (**e**) 600 °C for 1 day

[186], but it is sensible thinking that it is the result of the diffusionless, or partially diffusionless, transformation of nanostructured bainite, where vacancies would be playing a role [201].

The thermal stability of nanostructured bainite is tested by tempering experiments presented in Fig. 8.23. Tempering at 400 °C for 1 h does not introduce any perceptible change in the original microstructure, as shown in Fig. 8.23a, while the same treatment in nanostructured pearlite leads to spheroidization and coarsening of both ferrite and cementite (see Fig. 8.13d). Tempering at 450 °C for 1 h leads to decomposition of the austenite films by the precipitation of fine carbides (Fig. 8.23b), the length scale of the bainitic ferrite plates remaining intact. With increasing the tempering temperature to 550 °C, retained austenite decomposes completely, with larger austenite regions leading to cooperative growth of ferrite and cementite in the form of pearlite, which nucleates at cementite particles located at ferrite/austenite interfaces (Fig. 8.23c) [95]. Thus, carbon-rich austenite films are less thermally stable than austenite blocks due to both their higher amount of carbon in solid solution and the presence of higher amounts of carbon-containing defects [209]. Tempering of the original structure at 600 °C for 1 h produces major changes involving general coarsening, presented in Fig. 8.23d, and recrystallization when the heat treatment is prolonged to 1 day (Fig. 8.23e). It is thought that the resistance to tempering of nanostructured bainite is a consequence of carbide precipitation at the ferrite/austenite interface, which hinders the plate coarsening process [40, 74, 183].

8.4 Mechanical Performance of Nanostructured Steels

The ideal slip resistance of metals is about $G/30$, where G is the shear modulus of the material [27]. This level of strength is only achieved when the size of the crystal becomes sufficiently small. This was first demonstrated by Taylor, with the preparation of a 30 μm antimony wire whose tensile strength resulted in values about 30 times greater than those of 4 mm antimony crystals [243]. In the case of iron, crystals in the form of whiskers 1.6 μm in diameter have a yield strength of about 13.4 GPa and an ultimate tensile strength (UTS) of 16–23 GPa before fracture occurs [27]. The ideal strength of pure iron is thus computed to be around 13 GPa [43], and this value is dramatically decreased as materials scale-up [21]. It is in this context that the relationship between strength and nanoscale of current bulk nanostructured steels is examined.

8.4.1 Strength and Ductility of Nanostructured Pearlite

The highest tensile strengths that can be achieved in bulk material are found with eutectoid steels wires, where strength is routinely above 1.5 GPa but can reach more than 6 GPa [135]. In pearlitic steels, there are fundamentally four strengthening mechanisms: (1) Hall-Petch strengthening, (2) strain hardening, (3) solid solution hardening, and (4) dispersion hardening (only when cementite turns amorphous after large strains). In microstructural terms, the mechanical properties of pearlitic steels are mainly governed by the thickness of the cementite lamellae. In the case of cold-drawn pearlitic wires, stress-strain data presented in Fig. 8.24 indicate that two regimes are present: at true drawing strain, $\varepsilon \leq 3$ the strength increment as a function

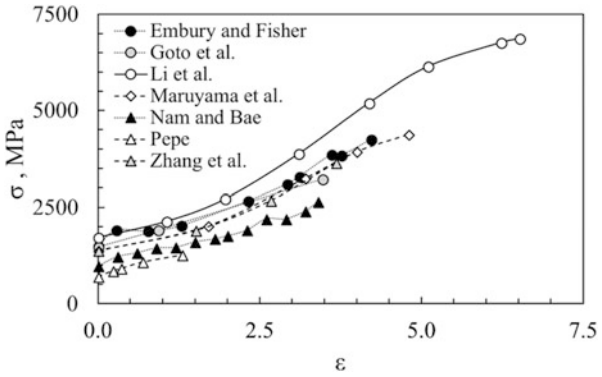

Fig. 8.24 Tensile strength, σ, for different true drawing strains, ε, as evaluated by different authors: Embury and Fisher [59], Goto et al. [86], Li et al. [136], Maruyama et al. [148], Nam and Bae [166], Pepe [185], and Zhang et al. [283]

of strain is lower, and increases when increasing strain presumably due to alignment of the cementite lamellae parallel to the drawing direction [167]. Therefore, the Hall-Petch strengthening is considered the most relevant mechanism in pearlitic steels, following the equation:

$$\Delta\sigma_{HP} = k\overline{L}^{-1/2} \tag{8.3}$$

where $k = 0.422$ MPa·m$^{1/2}$ is the Hall-Petch constant [265] and $\overline{L}$ is the effective grain size, corresponding to the interlamellar spacing S_0 in pearlitic steels. The concomitant strengthening effects of strain hardening, solid solution hardening, and dispersion hardening are remarkable for $\varepsilon \leq 2 - 3$ and are reviewed elsewhere [23]. The same strengthening mechanisms should apply to nanostructured pearlite produced by both cold drawing and solid reaction.

The fracture mechanism in pearlitic wires varies depending on the drawing strain. For $\varepsilon = 1 - 3$, the material undergoes ductile failure characterized by a cup and cone fracture accompanied by necking. This form of fracture occurs by the initial formation of microvoids in the interior of the material followed by microvoid enlargement and formation of a crack. As deformation continues, the crack grows rapidly spreading laterally toward the edges of the specimen forming an angle of 45° to the loading axis. The final shearing produces a cup type shape on one fracture surface and a matching cone shape on the other [23]. For wires cold drawn to $\varepsilon = 4 - 5$, observations indicate that fracture is ductile with the typical dimples indicating microvoid coalescence with a transition from a necking to the nonnecking mode between $\varepsilon = 3$ and $\varepsilon = 4$ [23, 86, 136].

8.4.2 *Temperature Dependence of Strength and Ductility of Nanostructured Ferritic Alloys*

Three dominant contributions are considered in the flow stress of ODS steels, namely, (1) Hall-Petch hardening due to the ferrite matrix, (2) hardening from dislocation forests, and (3) precipitation strengthening resulting from the oxide dispersoids. However, the superposition of these terms has been suggested to adopt a Pythagorean (rather a linear) superposition in the form [39]:

$$\sigma_Y = \sigma_{HP} + \sqrt{\sigma_\rho + \sigma_p} \tag{8.4}$$

where σ_Y is the yield strength, and σ_{HP}, σ_ρ, and σ_p are the Hall-Petch, dislocation forest, and nano-oxide precipitation strengthening contributions, respectively. For the first term, Hall-Petch hardening is considered to follow Eq. 8.3, with $k = 0.268$ MPa·m$^{1/2}$ [39, 191]. The contribution from dislocation strengthening is estimated by the Bailey-Hirsch relationship in terms of the forest intersection mechanism at the boundaries [39, 191]. Last but not least, nanoparticle strengthening adopts

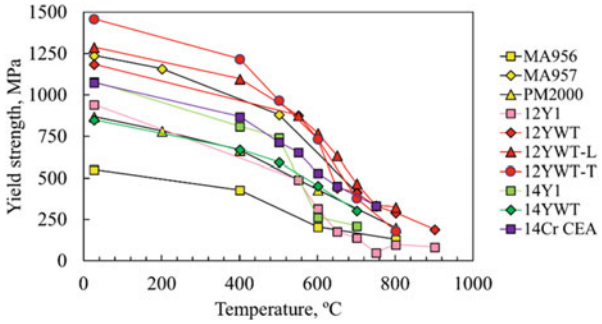

Fig. 8.25 Yield strength as a function of the testing temperature for various ODS steels and NFAs. The compositions of the alloys are given in Table 8.1, and the suffixes L and T indicate that samples were tested in the longitudinal and transversal directions, respectively. (Data adapted from [7, 57, 102, 121, 223])

different equations according to the particular dislocation-particle interaction mechanisms observed, which are strongly dependent on the type, size, shape, and coherency of the oxide. Under a general assumption [120, 262], oxide dispersion strengthening depends on the number density (N_p) and size (d_p) of the nanoparticles such that $\sigma_p \propto \sqrt{N_p d_p}$.

Figure 8.25 shows the yield strength as a function of the testing temperature for various conventional ODS steels (MA956 and PM2000) and NFAs, whose chemical composition is given in Table 8.1. Significant variations in the yield strength of the different steels are evidenced for testing temperatures below 800 °C; the lower the temperature the larger the difference. There is a general collapse of the tensile properties above 400 °C that can be explained by a change in the deformation mechanism. However, this behavior is interpreted in two different ways; some authors find that at the lowest temperatures, precipitates play a major role by pinning dislocation movement [39, 191], while others argue that the low-temperature properties are largely affected by the grain size and fraction of unrecrystallized material, where small atom clusters do not play a major role [7, 121]. At higher temperatures, the hardening role of the precipitates is still observed, until strength of all the alloys merges for extrapolations to 900 °C. The breakdown of the strength at elevated temperatures is due to control by other mechanisms. The strength depends in different ways on temperature, grain size, and strain rate [212]. Hence, the specific role of the nano-oxides in the strengthening of NFAs is complex and still needs to clarified from the point of view of both Hall-Petch strengthening by refining the ferrite matrix and precipitation strengthening itself.

Total elongation values presented in Fig. 8.26 as a function of the testing temperature for various conventional ODS steels and NFAs given in Table 8.1 indicate that ductility in these materials is relatively poor as compared to conventional steels. Most of the alloys show a peak in the elongation versus temperature at about 600–700 °C. At this temperature range, the deformation mechanism is modified, with an intragranular character turning into intergranular for higher temperatures. Damage

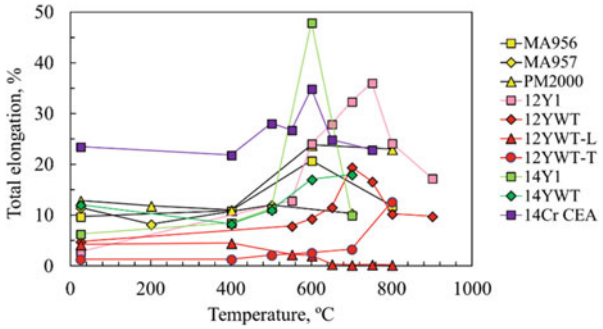

Fig. 8.26 Total elongation as a function of the testing temperature for various ODS steels and NFAs. The compositions of the alloys are given in Table 8.1, and the suffixes L and T indicate that samples were tested in the longitudinal and transversal directions, respectively. Data adapted from [7, 57, 102, 121, 223]

is more severe as the temperature is increased, particularly when the formation of cavities leading to decohesion along the grain boundaries starts [191].

8.4.3 Strength and Ductility of Nanostructured Bainite

Most of the strength in nanostructured bainite is the result of the bainitic ferrite plate thickness, t. As mentioned in the introduction, there is an inverse dependence of the strength on the effective grain size, which in this case corresponds to the true plate thickness as measured by mean linear intercept and follows the equation [129]:

$$\Delta\sigma = k\overline{L}^{-1} \tag{8.5}$$

where $k = 115$ MPa·μm and $\overline{L} = 2t$ [143]. The fact that strength does not obey the Hall-Petch relationship is because the transmission of slip across the effective grain boundaries is determined by the energy required to expand dislocation loops rather than by dislocation pile-up at the boundaries [129].

The total strength of ferrite alone is the result of (1) the plate thickness, (2) dislocation forests, (3) solid solution strengthening (including the carbon excess), and (4) carbide precipitates [20]. The strengthening contributions of these factors are minute as compared to that due to the bainitic ferrite plate size. This is held as a reason for the properties of the nanostructure to be insensitive to tempering, until the onset of plate coarsening [96].

Considering austenite alone, strength is simply described as a function of the composition and the temperature [278]. The strength of the whole ferrite plus austenite mixture in nanostructured bainite has been found to be mainly controlled

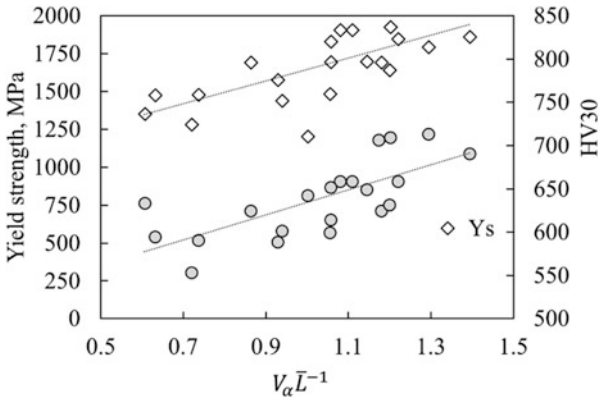

Fig. 8.27 Yield strength and hardness (HV30) of different bainite nanostructures as a function of $V_\alpha \bar{L}^{-1}$. V_α is the volume fraction of bainitic ferrite and $\bar{L} = 2t$, where t is the bainitic ferrite plate thickness. Adapted from [226–228]

by the inverse of the effective grain size weighted by the amount of the bainitic ferrite [71, 76], i.e., $V_\alpha \bar{L}^{-1}$, where V_α is the volume fraction of ferrite (Fig. 8.27).

Ductility in nanostructured bainite remains an unpredictable property, given that there is no correlation between the initial volume fraction and/or composition of austenite and the tensile ductility [159]. On the one hand, a large amount of unstable austenite is not appropriate for total elongation. On the other hand, a highly stable austenite, unable to undergo mechanically induced martensitic transformation, or implying a low rate of this transformation, is neither beneficial [161]. In this sense, microstructures exhibiting similar retained austenite contents and bainitic ferrite plate thickness, even produced from the same steel, show largely different tensile ductility [159, 226–228].

It has long been suggested that failure is a consequence of austenite isolation, i.e., failure occurs when austenite loses percolation. Modeling of this phenomenon, considering ellipsoidal objects placed in a matrix, predicts that the percolation threshold, and thus failure, occurs when $V_\alpha \approx 0.1$ [18]. Recently, a simple linear relationship has been recently proposed [229, 230] in an attempt to quantify, but not predict, the relationship between retained austenite stability and tensile ductility:

$$\ln\left(V_{\gamma,0}\right) - \ln\left(V_\gamma\right) \propto k\varepsilon_p \tag{8.6}$$

where $V_{\gamma,0}$ is the initial retained austenite content, V_γ is the retained austenite in the gauge length after applying a true plastic strain of ε_p, and k is a constant. Fittings to Eq. 8.6 in Fig. 8.28 indicate that values of k above 0.2 indicate rapid mechanical destabilization of austenite with increasing strain, leading to brittle fracture. Values of k below 0.2 are related to ductile fracture, with tensile elongation increasing as k is decreased. These results are conflicting with the suggested existence of a percolation threshold below which ductile deformation is no longer possible.

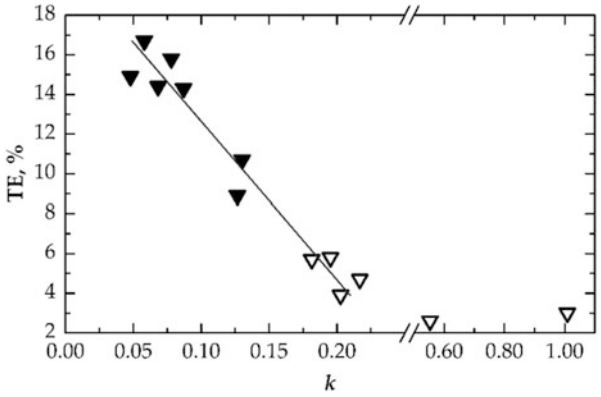

Fig. 8.28 Tensile elongation (TE) as a function of the value of k for different bainite nanostructures. Hollow symbols are for brittle ruptures; full symbols are for ductile ruptures, after [229, 230]

A general observation indicates that poor ductility is largely associated with the lowest transformation temperatures (about 220 °C), whereas transformation at slightly higher temperatures (about 250 °C) provide ductile behavior [229, 230]. The reduction of the mechanical mismatch between austenite and bainitic ferrite is speculated to be the reason behind the better performance of samples treated at higher temperature [160, 161].

Furthermore, recent studies show that mechanically induced martensitic transformation in nanostructured bainite is stress assisted, where mechanical twinning of austenite is not a necessary event prior to martensitic nucleation [162]. However, extensive twinning has been observed to occur in austenite blocks with a crystal orientation highly stable against martensitic transformation. Thus, both mechanically induced martensitic transformation and twinning contribute to plasticity and strain hardening in nanostructured bainite [162].

8.5 In-Use Properties and Industrial Applications of Nanostructured Steels

8.5.1 Applications and Failure Mechanisms in Nanostructured Pearlite Wire Ropes

Nanostructured pearlite wires are employed in a wide range of applications where a combination of ultra-high strength and sound ductility is required. The most relevant usages of drawn wires are tire cords, lifting ropes, and bridge cables [181], where individual wires are wither twisted or braided to form a rope. For both applications,

the design requirements rely on tensile and torsion strength, stiffness, ductility, corrosion resistance, and fatigue endurance of the drawn wires.

A wire rope or cable under tensile or bending loads places the individual wire elements in tension, torsion, and bending [65, 66]. The geometry of a strand of wire rope and its stress state under loading can acquire high levels of complexity, and they are of primary consideration for metallurgical development and tailoring of the properties. Effective design should minimize bending and torsion stresses and maximize axial stresses. Bending and torsion stresses can lead to splitting and delamination of the wire by inducing normal tensile stresses in the subsurface of the wire [28]. Furthermore, contact and cyclic stresses exist within each wire due to manufacturing and service loading [232]. For a proper design, torsion tests and fretting and fatigue behavior of the wires need to be effectively evaluated. The testing methodologies and properties of wire ropes and commercial cold drawn pearlitic wires are detailed elsewhere [65, 66]. Therefore, under normal circumstances, where no corrosion, excessive heat, severe overloading, or chemical damage is involved, failure of ropes occurs by either fatigue at the zones subjected to the greatest cyclic loading or abrasion [259]. This type of failure is predictable under proper inspection, given that individual wires fail first before the whole rope breaks down [260].

Besides, nanostructured pearlite wires are low alloyed, and corrosion resistance is thus poor. Wires exposed to environments where protection is needed are normally zinc coated by either hot zincing or galvanizing process. Only for exceptional cases, stainless steel wires are used as rope wires. Corrosion is a frequent failure in ropes when this occurs internally, i.e., when individual wires at the core of the rope do not receive proper protection preventing the inspector to foresee the problem [11]. Less common failure mechanism in ropes are those that cannot be predicted and usually lead to catastrophic failure, such as ropes "jumping the sheaves," lightning strikes, hydrogen embrittlement, and kinks [259].

For the reader to envision the magnitude of the requirements of nanostructured pearlite wires, a rousing example is given by Borchers and Kirchheim [23]: The Strait of Messina bridge is a suspension bridge projected to connect Torre Faro in Sicily and Villa San Giovanni in mainland Italy and designed to have the largest span in the world at 3.3 km. The suspension system of the bridge relies on two pairs of pearlitic steel cables, each of them having a diameter of 1.24 m and a total length of 5.3 km, corresponding to about 100 tons of steel cable alone. When considering the dynamic effects of traffic and an earthquake of 6.9 in the moment magnitude scale, the cables would be subjected to total deformations of more than 1 m or unitary strains of $3{\cdot}10^{-4}$. This value is far less than the elastic strain of nanostructured pearlite wires, which reaches a saturation value of 1.6% with increasing drawing strain. Thus, failure due to overloading is unlikely to occur in this class of material when design is safely performed.

8.5.2 *Industrial Applications and In-Use Properties of Nanostructured Ferritic Alloys*

The efficiency of plants that produce electric energy or heat is usually increased when the operation temperature is raised. Some examples requiring increased operation temperatures for improved efficiencies are gas and steam turbines, ultra-high temperature coal gasification, solar thermal applications, and advanced nuclear fusion and fission power plants. These latter are currently being studied within the framework of the International Generation IV initiative, where the sodium-cooled fast reactor (SFR) has received the greatest share of funding over the years. For the safe and efficient operation of the SFR, it is necessary to develop a clad material that meets the core specifications in terms of dimensions and surface finish, ductility, compatibility with helium coolant, and irradiation conditions at temperatures of 1000 °C during normal operation [12]. Besides, technologies and means for developing biomass plants with higher energy conversion efficiencies are essential to commit to renewable biomass energy generation in the future. Advanced, indirect combined cycle gas turbine (CCGT) systems offer overall biomass energy conversion efficiencies of 45% and above in comparison with the 35% efficiency of a conventional biomass steam plant. However, to attain this efficiency in CCGT operations, it is necessary to develop a heat exchanger capable of gas-operating temperatures of approximately 1100 °C and pressures of 15–30 bar. Current structural steels and superalloys are at the limits of their applicability under such severe environments, and the development of components with improved performance remains a strong driving force for further progress. ODS steels are candidate materials for use in these next-generation high-temperature applications.

8.5.2.1 Oxidation and Corrosion Resistance of Nanostructured Ferritic Alloys

In the case of ODS ferritic steels containing ~5 wt.% Al, such as PM2000 and MA956, an α-alumina scale forms upon high-temperature exposure, which acts as a good barrier against oxidation [51, 147, 152, 267]. In cases of exposure to environments with low-oxygen content, formation of the protective layer is not guaranteed, but a preoxidation treatment, i.e., oxidation of the alloy prior to exposure, can be applied [69, 90]. Besides their good oxidation resistance, PM2000 and MA956 ODS steels present an outstanding creep performance [231]. On the contrary, the absence of aluminum in the 12YWT and 14YWT NFAs makes them susceptible to corrosion under certain media, such as liquid lead-bismuth eutectic cooled reactors and spallation sources, where aluminum-containing ODS steels show an excellent performance [106]. It is worth mentioning that a decreased grain size plays a positive role against localized oxidation, given that grain boundaries act as fast diffusion paths inside the material preventing deep localized grain boundary oxidation [61, 106].

8.5.2.2 Creep Resistance of Nanostructured Ferritic Alloys

Besides the homogeneous dispersion of nanosized oxides in the ferritic matrix, ODS ferritic steels and NFAs usually exhibit high-strength and creep resistance properties as a consequence of being far from the equilibrium state [3, 83]. Many features, such as a large proportion of interfaces and triple junctions, irregular distributions of alloying elements, the occurrence of nonequilibrium phases and supersaturated solutions, residual stresses, and excess concentrations of lattice defects, increase the Gibbs free energy. All these features are closely connected with the nonequilibrium conditions of the ODS fabrication methods by powder technology [87, 144]. The excellent creep properties of the NFAs are due to an attractive interaction of dislocations with oxides described in the well-known model by Rösler and Arzt [203]. Creep usually exhibits the threshold stress, which correlates well with the Orowan theory according to which, at a given temperature, the threshold stress is inversely proportional to the distance of the oxides. Thus, any coarsening of the oxides causes a degradation of the creep properties.

Figure 8.29 illustrates the superior creep performance of different ODS steels, and specially of the MA957, 12YWT, and 14YWT NFAs, as compared with the 9Cr TMP steel having similar chemical composition but not reinforced with oxide particles. Creep resistance is here expressed by means of the Larson-Miller parameter (LMP), which allows predicting the lifetime of material vs. time and temperature using a correlative approach based on the Arrhenius rate equation. The value of the parameter is usually expressed as $\mathrm{LMP} = T(c + \log t)$, where c is a material specific constant, approximated as values between 20 and 30, t is the time in hours, and T is the temperature in Kelvin.

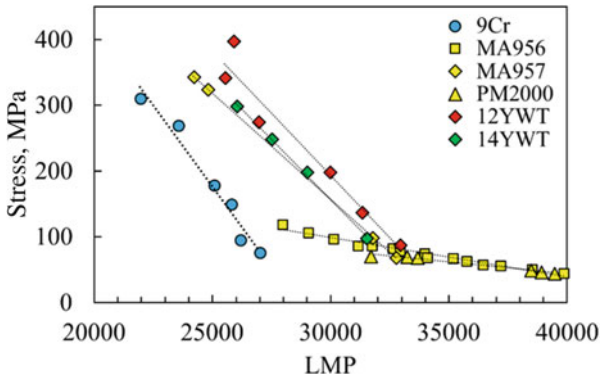

Fig. 8.29 Larson Miller parameter (LMP) for various conventional ODS steels and NFAs. (Data adapted from [102, 121])

8.5.2.3 Irradiation Resistance of Nanostructured Ferritic Alloys

Irradiation resistance in NFAs is obtained two ways. First, they contain highly stable dislocation sinks with a large number density of thermally stable, nanometer-scale precipitates that trap helium in bubbles to avoid swelling and helium migration to the matrix grain boundaries with the subsequent intergranular fracture. Second, they present high creep strength, permitting operation at temperatures above the displacement damage regime. These two characteristics are responsible for the superior irradiation resistance of ODS steels and NFAs as compared to thermomechanically processed heat resistant steel that do not contain nano-oxide precipitates. As long as NFAs are operated at temperatures above the displacement damage-swelling regime, they are able to manage very high helium levels, reaffirming their suitability for fusion reactor structures. An extensive overview of the irradiation damage in these and other heat-resistant steels can be found in [99, 175].

8.5.2.4 Scalability of Nanostructured Ferritic Alloys

The key point for the rather feeble industrial application may be that producing NFAs and ODS by the current PM route is certainly expensive. Even if the high costs could be justified by the absence of materials with comparable properties, the potential applications need to be established for manufacturers[3] to emerge and promote the development of this class of alloys. For this reason, applications cannot be limited to the niche of nuclear fusion and fission power plants but to systems where there is room for increases in the operation temperatures, as previously introduced. Anyhow, NFAs are used in applications requiring small amounts of material in complex multimaterial hybrid systems. A perspective of cost is given by Odette [174] for a first wall and divertor hybrid structure in a large demonstration fusion reactor requiring 10 tons of NFA at a target price of $50/kg for consolidated billets. The cost of the material alone would be of five million dollars, remaining a small fraction of the total cost of a 10,000 million dollar fusion power reactor. Even though the cost of construction does not reflect the global cost of electric power economics (including the environmental cost), it is thought that the use of either ODS steels or NFAs is a feasibility enabling issue [174].

[3]The production of MA957 was discontinued by INCO, and so it was the production of PM2000 by Plansee, while 12YWT was produced only once as a small heat by Kobe steel.

8.5.3 *Industrial Applications and Failure Mechanisms of Nanostructured Pearlite Produced by Solid Reactions*

The main industrial use of fully pearlitic structures is in rail steels. The first steel rail to be ever used is said to be the one laid in Derby station on the Midland Railway in 1857 [277] when no one even knew what pearlite is. The essential microstructure of those rails was similar to that of the rail steels used today, pearlitic structures based on nearly eutectoid compositions. Of course improvements have been made in the last 150 years in order to enhance the basic features around the fundamental structure by optimizing the chemical composition and impurity/cleanliness levels and by controlling the austenitization temperatures and cooling paths that lead to microstructural refinement [233].

The main failure mechanism in rails is wear caused by rolling contact fatigue arising from cyclic loading at the railhead. The main stress components at the rails are the rolling contact pressure, shear, and bending forces due to certain sliding in the rail/wheel contact, and residual stresses arising from manufacturing and welding. Less relevant failure considerations are related to overloads and harsh environmental conditions [222].

In eutectoid pearlitic steels, fatigue strength is found to be insensitive to the interlamellar spacing [52]. However, reduced pearlite interlamellar spacings have a greater flow stress and work-hardening rate [237], both of which lead to a reduction in the wear rate [44, 187, 237]. The strong correlation between the wear resistance and the interlamellar spacing (also reflected an increase in hardness) has led to processing and alloying approaches to produce fine fully pearlitic structures.

Figure 8.30 shows the specific-wear resistance as a function of the hardness of the nanostructured pearlite as compared to somewhat softer pearlitic steels and a variety of bainitic steels, some of which are much harder [53, 226–228]. The results emphasize the fact that wear performance cannot be simply estimated on the basis of phase fractions or hardness when the mechanisms of wear are dependent on microstructural parameters.

An effective and widely used processing approach to produce refined pearlitic structure on the surface of the rails is the *head hardening* heat treatment [204]. Head hardening is applied by accelerated cooling with forced air, water sprays, or oil or aqueous polymer quenching either in the production line while the steel is still austenitic immediately after hot rolling [26] or separately by reheating of as-rolled rails [205]. Accelerated cooling is applied so that a refined pearlitic microstructure is obtained at the railhead where the rolling contact and sliding occur. By careful adaption of both the steel composition and the thermal history during head hardening, it is currently feasible to obtain pearlite nanostructures in an industrial environment [25].

Nevertheless, it should be emphasized that the steel rail industry is strongly cost driven, and while microalloying with expensive elements such as vanadium or molybdenum is admitted, relatively high cobalt additions as those proposed in [53, 271, 272] are simply inconceivable. Also, pearlite formed under isothermal

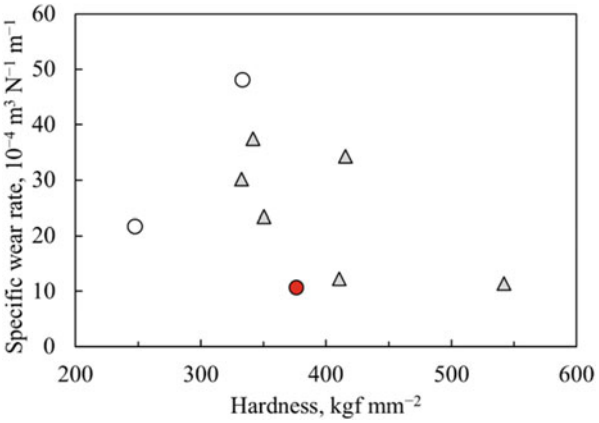

Fig. 8.30 Specific wear rates as a function of the initial hardness measured in rolling/sliding tests. The triangles represent bainitic steels, circles correspond to pearlitic steels, and the filled point is nanostructured pearlite. Data estimated from [53, 226–228]

conditions near the B_S temperature exhibits the finest achievable interlamellar spacing for a given composition (illustrated in Fig. 8.3 for patented wires). Unlike for sheets, for which the rolling and coiling operations ease isothermal transformations, long product manufacturing routes are not typically suited for controlled cooling followed by isothermal paths.

With the development of heavy-load high-speed railways, the in-use demands for rails are increasingly pushing current metallurgical approaches to their limits. Safety and cost of railway transportations are partly related to the quality of rail steel, and improved nanostructures with reliable damage tolerance design and effective maintenance methods are under continuous development.

8.5.4 In-Use Properties and Industrial Applications of Nanostructured Bainite

Nanostructured bainite has attracted considerable attention over the past 15 years, far from but getting closer to industrial applications. Research efforts have focused on evaluating the in-use performance of these materials for various applications implying mainly fatigue and wear resistance, beyond looking at basic tensile strength. This implies understanding the microstructure-properties relationships and also comparing the results to currently used steel grades and other manufacturing methods for such applications as well as evaluating the costs of the different alternatives.

Until today, the Research Fund for Coal and Steel (RFCS) of the European Commission has financially supported three projects aimed at the industrialization

of nanostructured bainite, namely Nanobain [226–228], Mecbain [229, 230], and more recently Bainwear [192]. These were consortia gathering scientists, steel makers, and end users sharing a common intrigue and interest for the bainitic nanostructures and ended up with unique developments in understanding both the physical metallurgy and properties of these steels.

The evaluation of the notched fatigue performance for a variety of load ratios and notch severity of nanostructured bainite isothermally transformed at 220 or 250 °C to a UTS over 2 GPa shows that the materials behave 10–20% better than 100Cr6 isothermally transformed to a UTS of 2.35 GPa [76, 226–228]. The fatigue response of nanostructured bainite is strongly dependent on cleanliness (as for most high-strength steels) and the crystallographic grain size as the critical microstructural parameter [164, 197] (Table 8.2).

Wear resistance of nanostructured bainite is far more promising with significant improvements under specific dry sliding, dry rolling-sliding, and rolling contact fatigue conditions [131, 198]. As a general conclusion, for each wear system the nanostructures can be optimized by adjusting the amount, size, distribution, and stability of phases. To this end, the specific and synergistic role of each phase in the wear mechanisms must be first understood.

Field tests have been recently carried out to assess the suitability of bainite nanostructures in rollers, punches, bearings, and reducing elements [192], and the results are summarized as follows: Guide rollers for rolling mills made of nanostructured materials show better performance in warm applications than current grades (see Fig. 8.31), although they do not offer advantages in Calow straightener rollers in cold applications. In the case of sheet metal cutting punches, nanostructured bainite performs favorably when used in extremely harsh conditions, outperforming

Table 8.2 Tensile properties and fatigue data for different loading and notch conditions for various nanostructured bainitic steels and reference materials (50CrMo4 and 100Cr6). Results underline the excellent performance of the 0.6C-1.5Si under both isothermal treatment conditions. YS is the 0.2% offset yield strength, UTS is the ultimate tensile strength, UE is the uniform elongation, TE is the total elongation, $S_{a,\,50\%}$ is the fatigue strength for a probability of failure of 50% (mean value) at 10^7 cycles, R is the maximum to minimum stress ratio, and K_t is the stress concentration factor. Adapted from [229, 230]

						$S_{a,\,50\%}$, MPa		
						$K_t = 2$		$K_t = 4$
Variant	Isothermal treatment	YS, MPa	UTS, MPa	UE, %	TE, %	R = 0.1	R = -1	R = 0.1
0.6C-1.5Si	220 °C 114 h	1643	2102		4.5	350	605	240
0.6C-1.5Si	250 °C 16 h	1448	1990	8.2	14.3	365	605	230
0.6C-2.5Si	250 °C 16 h	1483	1950	8.1	8.6	255	–	–
1C-1.5Si	250 °C 16 h	1740	2170	8.8	10.7	310	–	–
1C-2.5Si	250 °C 16 h	1738	2106	11.7	16.8	310	445	210
1C-2.5Si	250 °C 40 h	1785	2101	4.3	15.8	335	420	200
50CrMo4	To 37 HRC	1118	1183	5.1	14.7	305	333	
100Cr6		2150	2350			355	566	200

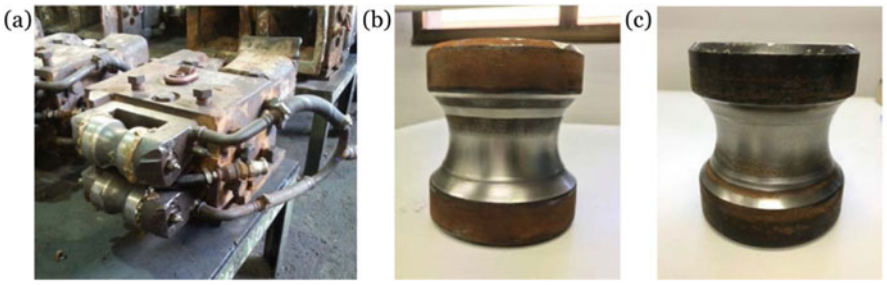

Fig. 8.31 (**a**) Set-up of the vertical guide rolls located at the entrance of the hot rolling stage in order to facilitate the passage of the bars, (**b**) nanostructured bainite guide roll, and (**c**) undisclosed pearlitic roll, which is the current main alternative. Measurements with a template, evaluation of weight loss, and comparison of flank profiles all show an advantage of nanostructured bainite rollers. (Adapted from [192])

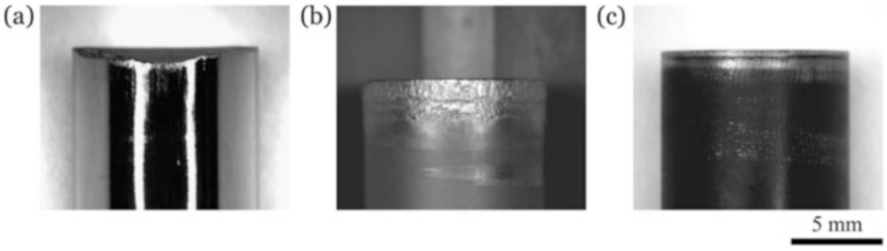

Fig. 8.32 Images of selected punches: (**a**) Reference DIN 1.2379 in quench and tempered conditions, showing severe chipping at the tip and failure after 10 cycles, (**b**) nanostructured bainitic steel uncoated showing wear and blunting of the cutting surface but no failure before 850 cycles, and (**c**) coated nanostructured bainitic steels showing almost no wear and no failure after 850 cycles. (Adapted from [192])

the reference DIN1.2379 tool steel, as illustrated in Fig. 8.32. Nanostructured bainite bearing components tested under artificial pollution outperform the reference 100Cr6 material, with a significant margin of benefit. Finally, trials on reducing elements were not conclusive, and under the studied conditions, nanostructured bainite grades did not offer advantages over the conventional 1.2379 material, where the wear mechanisms proved to be very different; this was considered interesting for further applications.

In contrast with its intense academic research activity, nanostructured bainite is still far from mass production for two main reasons [225]. First, the heat-treatment remains complex and commonly requires the use of salt baths with the finest temperature control. Such installations are far less frequent than conventional and simpler quenching and tempering furnaces. Furthermore, existing lines are often designed to handle treatments significantly shorter than those required to produce nanostructured bainite. Second, the benefits remain to be undoubtedly established. In particular, for components where fatigue is the main damage mechanism,

nanostructured bainite should bring a sufficiently large advantage to justify a change from existing solutions. For components where wear is the main damage mechanism, it is firmly established that bainite nanostructures have exceptional potential, but further work is required before they can be transferred to actual applications.

With regard to heat treatment durations needed for isothermal transformation, several attempts have been made to improve the reaction kinetics. These have been focused in modifications of the composition [72, 73, 226–228] and heat-treatment schedules, e.g., by producing partial martensite transformation before subsequent isothermal bainite transformation [85] or by multistep isothermal heat treatments [138, 139]. A new approach is currently being explored under the auspices of the RFCS-funded project, Tianobain [70], where leaner medium-carbon alloys and shorter-processing times via thermomechanical ausforming are expected to lead to at least ultrafine bainitic steels with tensile strengths above 1600 MPa [78]. Trial products will be produced and tested using laboratory rolled materials, and recommendations for full-scale production parameters will be made.

Independent of commercial developments, nanostructured bainite can be considered as the upper limit of nanostructures obtained by solid-solid phase transformations, and their study is key for further improvements and understanding of this class of materials.

8.6 Future Trends

The set of *enabling technologies* that will supposedly lead us to the so-called *Industry 4.0* or the fourth Industrial Revolution, enabling the complete digitization of most industrial processes include cognitive and cloud computing, cyber-physical systems, virtual reality, the Internet of Things, big data, and last but not least, additive manufacturing [213]. Additive manufacturing is attracting much attention in the field of metallurgy, owing to the potential for direct manufacturing of complex parts which would not be possible to machine using current methods. Relevant additive manufacturing processes for metals consist in successively depositing wire or powder material that is locally melted on the top surface of the sample to add a new layer. This is achieved by selectively melting the material deposited using an energetic electron or laser beam. The technology is currently being used in rapid prototyping, cladding, coating, tooling and parts repair, and screening of novel alloys or functionally graded materials.

The main additive manufacturing processes for steels, both selective laser melting (SLM) and direct energy deposition (DED), consist in local melting and solidification of the steel powder. In principle, the structures obtained can be controlled through the process parameters, i.e., the laser power, the speed, and the hatch distance or the distance in between two laser passes. To fully understand the correlation between the microstructure and the thermal history, efforts are put to

measure the temperatures of the melted zones and the cooling rates in situ [15, 62], which are often said to be in the overwhelming range of 10^4–10^6 °C/s for SLM.

The very particular, powder-metallurgical and nonequilibrium characteristics of additive manufacturing processing leaves room to alloys and micro/nanostructures that are not accessible through classical metallurgical routes. This includes supersaturated solid solutions, suppression of unwanted phase precipitation, composite synthesis, and in situ metal-gas reactions. Indeed, SLM-processed parts have completely different microstructures to those found in cast or wrought steel, which are not even recognizable for an experienced metallurgist. Phase distribution and dislocation network structures arising from the rapid solidification process are quite unique and different from the microstructures and dislocation cells observed in deformed metals. The resulting tensile properties in bulk steel parts additively produced are usually superior than those of wrought or cast material [119, 138, 139, 224].

The benefits of rapid solidification can be exploited by careful alloying as a method to promote massive heterogeneous nucleation and lower the energy of grain boundaries, bringing stable nanocrystalline steel structures. The opportunities that additive manufacturing bring in producing not only nanostructured but a new range of steels have not yet been exploited. Actually, the materials portfolio for metal additive manufacturing only includes a few stainless and tool steels having the standard composition of the wrought or cast grades. The race for new steel compositions adapted to the process is running for both scientist and the main powder manufacturers. Until now, there are no innovative solutions available in the market. The most remarkable work on steels specifically designed for additive manufacturing being that developed in the Max Planck Institute in conjunction with the Fraunhofer Institute for Laser Technology [128].

Besides, the myth that of 3-D printing in metal will allow producers to replace mass manufacturing with mass customization needs to be dispelled [22]. Additive manufacturing will be a disruptive technology in the sense that it will allow to produce complex steel parts with graded mechanical properties [142, 215] which cannot be achieved by conventional means, but replacing of traditional manufacturing techniques is not expected at least in the upcoming decades. If any, hybrid manufacturing approaches combining both mass conventional processing and additive manufacturing are a prospect [234]. Thus, the development and understanding of bulk nanostructured steels that can be produced by the classical routes is expected to keep in vogue.

8.7 Sources of Further Information

All the findings and developments carried out in nanostructured steels since their appearance do not fit in this chapter, and each of the metallurgical concepts well deserves its own book. Here there are some useful references where the reader can taste the complexity and beauty of each of the topics: bulk nanostructured materials

(general) [254, 266, 281]; pearlitic steel wires [23, 64, 270]; pearlite and rails [34, 89, 134, 180, 193, 240]; nanostructured bainite [19, 226–230]; and NFAs and heat-resistant steels [154, 155, 217, 264, 279].

Acknowledgements The authors acknowledge financial support from the Spanish Ministerio de Economia y Competitividad (MINECO) in the form of a coordinate project (MAT2016-80875-C3-1-R) and the Research Fund for Coal and Steel of the European Commission under the contract SuperHigh (RFSR-CT-2014-00019).

References

1. M. J. Alinger, On the Formation and Stability of Nanometer Scale Precipitates in Ferritic Alloys during Processing and High Temperature Service. Doctor of Philosophy, University of California (2004)
2. M.J. Alinger, G.R. Odette, D.T. Hoelzer, On the role of alloy composition and processing parameters in nanocluster formation and dispersion strengthening in nanostuctured ferritic alloys. Acta Mater. **57**(2), 392–406 (2009)
3. R.A. Andrievskii, A.M. Glezer, Size effects in nanocrystalline materials: I. structure characteristics, thermodynamics, phase equilibria, and transport phenomena. Phys. Met. Metallogr. **88**(1), 45–66 (1999)
4. B.M. Arkhurst, J.H. Kim, Evolution of microstructure and mechanical properties of oxide dispersion strengthened steels made from water-atomized Ferritic powder. Met. Mater. Int. **24**(3), 464–480 (2018)
5. E.G. Astafurova, G.G. Zakharova, E.V. Naydenkin, S.V. Dobatkin, G.I. Raab, Influence of equal-channel angular pressing on the structure and mechanical properties of low-carbon steel 10G2FT. Phys. Met. Metallogr. **110**(3), 260–268 (2010)
6. J.M. Atienza, M. Elices, J. Ruiz-Hervias, L. Caballero, A. Valiente, Residual stresses and durability in cold drawn eutectoid steel wires. Met. Mater. Int. **13**(2), 139–143 (2007)
7. M.A. Auger, V. de Castro, T. Leguey, M.A. Monge, A. Muñoz, R. Pareja, Microstructure and tensile properties of oxide dispersion strengthened Fe–14Cr–0.3Y2O3 and Fe–14Cr–2W–0.3Ti–0.3Y2O3. J. Nucl. Mater. **442**(Supplement 1), S142–S147 (2013)
8. E. Aydogan, S.A. Maloy, O. Anderoglu, C. Sun, J.G. Gigax, L. Shao, F.A. Garner, I.E. Anderson, J.J. Lewandowski, Effect of tube processing methods on microstructure, mechanical properties and irradiation response of 14YWT nanostructured ferritic alloys. Acta Mater. **134**, 116–127 (2017)
9. E. Aydogan, O. El-Atwani, S. Takajo, S.C. Vogel, S.A. Maloy, High temperature microstructural stability and recrystallization mechanisms in 14YWT alloys. Acta Mater. **148**, 467–481 (2018)
10. M.M. Baloch, H.K.D.H. Bhadeshia, Directional recrystallisation in Inconel MA 6000 nickel base oxide dispersion strengthened superalloy. Mater. Sci. Technol. UK **6**(12), 1236–1246 (1990)
11. P. Barnes, T. McLaughlin, Corrosion fatigue behaviour of high strength steel wire in various aqueous environments. NACE - International Corrosion Conference Series. 2015-January (2015)
12. C. Behar, Technology roadmap update for generation IV nuclear energy systems. E. N. E. A. f. t. G. I. I. Forum. **17**, 2014–2003 (2014)
13. J.S. Benjamin, Dispersion strengthened superalloys by mechanical alloying. Metall. Trans. **1**(10), 2943–2951 (1970)
14. F. Bergner, I. Hilger, J. Virta, J. Lagerbom, G. Gerbeth, S. Connolly, Z. Hong, P.S. Grant, T. Weissgärber, Alternative fabrication routes toward oxide-dispersion-strengthened steels and model alloys. Metall. Mater. Trans. A Phys. Metall. Mater. Sci. **47**(11), 5313–5324 (2016)

15. U.S. Bertoli, G. Guss, S. Wu, M.J. Matthews, J.M. Schoenung, In-situ characterization of laser-powder interaction and cooling rates through high-speed imaging of powder bed fusion additive manufacturing. Mater. Des. **135**, 385–396 (2017)
16. H.K.D.H. Bhadeshia, A rationalisation of shear transformations in steels. Acta Metall. **29**(6), 1117–1130 (1981)
17. H. Bhadeshia, Recrystallisation of practical mechanically alloyed iron-base and nickel-base superalloys. Mater. Sci. Eng. Struct. Mater. Prop. Microstruct. Proces. **223**(1–2), 64–77 (1997)
18. H. Bhadeshia, Properties of fine-grained steels generated by displacive transformation. Mater. Sci. Eng. A **481**, 36–39 (2008)
19. H.K.D.H. Bhadeshia, *Bainite in Steels: Theory and Practice* (Maney Publishing, 2015)
20. H.K.D.H. Bhadeshia, J.W. Christian, Bainite in steels. Metall. Trans. **A 21 A**(4), 767–797 (1990)
21. H.K.D.H. Bhadeshia, H. Harada, High-strength (5 GPa) steel wire: An atom-probe study. Appl. Surf. Sci. **67**(1), 328–333 (1993)
22. J. Bonnín-Roca, P. Vaishnav, J. Mendonça, G. Morgan, Getting past the hype about 3-D printing. MIT Sloan Manag. Rev. **58**(3), 57 (2017)
23. C. Borchers, R. Kirchheim, Cold-drawn pearlitic steel wires. Prog. Mater. Sci. **82**, 405–444 (2016)
24. X. Boulnat, N. Sallez, M. Dadé, A. Borbély, J.L. Béchade, Y. De Carlan, J. Malaplate, Y. Bréchet, F. De Geuser, A. Deschamps, Influence of oxide volume fraction on abnormal growth of nanostructured ferritic steels during non-isothermal treatments: An in situ study. Acta Mater. **97**, 124–130 (2015)
25. B. Bramfitt, F. Fletcher, A Perspective on the Manufacture of Modern-Day High-Strength Steel Rail. AREMA 2013 Annual Conference, Indianapolis (2013)
26. B.L. Bramfitt, R.L. Cross, D.P. Wirick, Advanced in-line head hardening of rail. Iron Steelmak. **22**(1), 17–21 (1995)
27. S.S. Brenner, Tensile strength of whiskers. J. Appl. Phys. **27**(12), 1484–1491 (1956)
28. A. Brownrigg, R. Boelen, M. Toyama, Delamination of hard drawn eutectoid steel, in *Fracture 84*, ed. by S. R. Valluri, D. M. R. Taplin, P. R. Rao, J. F. Knott, R. Dubey, (Pergamon, 1984), pp. 1431–1438
29. T.S. Byun, J.H. Yoon, D.T. Hoelzer, Y.B. Lee, S.H. Kang, S.A. Maloy, Process development for 9Cr nanostructured ferritic alloy (NFA) with high fracture toughness. J. Nucl. Mater. **449**(1), 290–299 (2014)
30. F.G. Caballero, M.K. Miller, S.S. Babu, C. Garcia-Mateo, Atomic scale observations of bainite transformation in a high carbon high silicon steel. Acta Mater. **55**(1), 381–390 (2007)
31. F.G. Caballero, C. Garcia-Mateo, M.J. Santofimia, M.K. Miller, C. García de Andrés, New experimental evidence on the incomplete transformation phenomenon in steel. Acta Mater. **57**(1), 8–17 (2009)
32. F.G. Caballero, M.K. Miller, C. Garcia-Mateo, Carbon supersaturation of ferrite in a nanocrystalline bainitic steel. Acta Mater. **58**(7), 2338–2343 (2010)
33. F.G. Caballero, M.K. Miller, C. Garcia-Mateo, J. Cornide, M.J. Santofimia, Temperature dependence of carbon supersaturation of ferrite in bainitic steels. Scr. Mater. **67**(10), 846–849 (2012)
34. J.W. Cahn, W.C. Hagel, Theory of the Pearlite Reaction, in *The Selected Works of John W. Cahn*, (1998), pp. 133–198
35. C. Capdevila, Y.L. Chen, N.C.K. Lassen, A.R. Jones, H. Bhadeshia, Heterogeneous deformation and recrystallisation of iron base oxide dispersion strengthened PM2000 alloy. Mater. Sci. Technol. **17**(6), 693–699 (2001)
36. C. Capdevila, Y.L. Chen, A.R. Jones, H. Bhadeshia, Grain boundary mobility in Fe-base oxide dispersion strengthened PM2000 alloy. ISIJ Int. **43**(5), 777–783 (2003)
37. C.E. Carlton, P.J. Ferreira, What is behind the inverse Hall–Petch effect in nanocrystalline materials? Acta Mater. **55**(11), 3749–3756 (2007)

38. J. Chao, R. Rementeria, M. Aranda, C. Capdevila, J.L. Gonzalez-Carrasco, Comparison of ductile-to-brittle transition behavior in two similar ferritic oxide dispersion strengthened alloys. Materials **9**(8), 637 (2016)
39. A. Chauhan, F. Bergner, A. Etienne, J. Aktaa, Y. de Carlan, C. Heintze, D. Litvinov, M. Hernandez-Mayoral, E. Oñorbe, B. Radiguet, A. Ulbricht, Microstructure characterization and strengthening mechanisms of oxide dispersion strengthened (ODS) Fe-9%Cr and Fe-14%Cr extruded bars. J. Nucl. Mater. **495**, 6–19 (2017)
40. C.-Y. Chen, Microstructure characterization of nanocrystalline bainitic steel during tempering. J. Alloys Compd. **762**, 340–346 (2018)
41. T.S. Chou, H. Bhadeshia, Grain control in mechanically alloyed oxide dispersion-strengthened Ma-957 steel. Mater. Sci. Technol. **9**(10), 890–897 (1993)
42. T.S. Chou, H.K.D.H. Bhadeshia, Recrystallization temperatures in mechanically alloyed oxide-dispersion-strengthened MA956 and MA957 steels. Mater. Sci. Eng. A **189**(1), 229–233 (1994)
43. D.M. Clatterbuck, D.C. Chrzan, J.W. Morris, The ideal strength of iron in tension and shear. Acta Mater. **51**(8), 2271–2283 (2003)
44. P. Clayton, D. Danks, Effect of interlamellar spacing on the wear resistance of eutectoid steels under rolling-sliding conditions. Wear **135**(2), 369–389 (1990)
45. H. Conrad, J. Narayan, On the grain size softening in nanocrystalline materials. Scr. Mater. **42**(11), 1025–1030 (2000)
46. J. Cornide, C. Garcia-Mateo, C. Capdevila, F.G. Caballero, An assessment of the contributing factors to the nanoscale structural refinement of advanced bainitic steels. J. Alloys Compd. **577**, S43–S47 (2013)
47. A.L.M. Costa, A.C.C. Reis, L. Kestens, M.S. Andrade, Ultra grain refinement and hardening of IF-steel during accumulative roll-bonding. Mater. Sci. Eng. A **406**(1), 279–285 (2005)
48. F. Cruz-Gandarilla, A.M. Salcedo-Garrido, M. Avalos, R. Bolmaro, T. Baudin, J.G. Cabañas-Moreno, H.J. Dorantes-Rosales, *EBSD Characterization of an IF Steel Processed by Accumulative Roll Bonding* (IOP Publishing, n.d.)
49. N. Cunningham, Y. Wu, D. Klingensmith, G.R. Odette, On the remarkable thermal stability of nanostructured ferritic alloys. Mater. Sci. Eng. A **613**, 296–305 (2014)
50. N.J. Cunningham, M.J. Alinger, D. Klingensmith, Y. Wu, G.R. Odette, On nano-oxide coarsening kinetics in the nanostructured ferritic alloy MA957: A mechanism based predictive model. Mater. Sci. Eng. A **655**, 355–362 (2016)
51. A. Czyrska-Filemonowicz, D. Clemens, W.J. Quadakkers, The effect of high temperature exposure on the structure and oxidation behaviour of mechanically alloyed ferritic ODS alloys. J. Mater. Process. Tech. **53**(1–2), 93–100 (1995)
52. M.d.G.M. da Fonseca Gomes, L.H. de Almeida, L.C.F.C. Gomes, I. Le May, Effects of microstructural parameters on the mechanical properties of eutectoid rail steels. Mater. Charact. **39**(1), 1–14 (1997)
53. S. Das Bakshi, A. Leiro, B. Prakash, H.K.D.H. Bhadeshia, Dry rolling/sliding wear of nanostructured pearlite. Mater. Sci. Technol. **31**(14), 1735–1744 (2015)
54. A. Das, H.-W. Viehrig, E. Altstadt, F. Bergner, J. Hoffmann, Why do secondary cracks preferentially form in hot-rolled ODS steels in comparison with hot-extruded ODS steels? Crystals **8**(8), 306 (2018)
55. J. De Messemaeker, B. Verlinden, J. Van Humbeeck, Texture of IF steel after equal channel angular pressing (ECAP). Acta Mater. **53**(15), 4245–4257 (2005)
56. C. Doñate-Buendía, F. Frömel, M.B. Wilms, R. Streubel, J. Tenkamp, T. Hupfeld, M. Nachev, E. Gökce, A. Weisheit, S. Barcikowski, F. Walther, J.H. Schleifenbaum, B. Gökce, Oxide dispersion-strengthened alloys generated by laser metal deposition of laser-generated nanoparticle-metal powder composites. Mater. Des. **154**, 360–369 (2018)
57. P. Dubuisson, Y.d. Carlan, V. Garat, M. Blat, ODS Ferritic/martensitic alloys for sodium fast reactor fuel pin cladding. J. Nucl. Mater. **428**(1), 6–12 (2012)
58. M. Durand-Charre, *Of Swords and Swordmaking. Microstructure of Steels and Cast Irons* (Springer, 2004), pp. 13–34

59. J.D. Embury, R.M. Fisher, The structure and properties of drawn pearlite. Acta Metall. **14**(2), 147–159 (1966)
60. M. Enomoto, W. Huang, H. Ma, Modeling pearlite transformation in super-high strength wire rods: II. Simulation in Fe–C Base multi-component alloys. ISIJ Int. **52**(4), 632–637 (2012)
61. J. Farmer, B. El-dasher, J. Ferreira, M. S. d. Caro, A. Kimura, Coolant Compatibility Studies for Fusion and Fusion-Fission Hybrid Reactor Concepts: Corrosion of Oxide Dispersion Strengthened Iron-Chromium Steels and Tantalum in High Temperature Molten Fluoride Salts, Lawrence Livermore National Lab.(LLNL), Livermore, CA (United States) (2010)
62. M.H. Farshidianfar, A. Khajepour, A.P. Gerlich, Effect of real-time cooling rate on microstructure in laser additive manufacturing. J. Mater. Process. Technol. **231**, 468–478 (2016)
63. C. Fazio, A. Alamo, A. Almazouzi, S. De Grandis, D. Gomez-Briceno, J. Henry, L. Malerba, M. Rieth, European cross-cutting research on structural materials for generation IV and transmutation systems. J. Nucl. Mater. **392**(2), 316–323 (2009)
64. K. Feyrer, *Wire Ropes* (Springer, 2007)
65. K. Feyrer, Wire Ropes Under Tensile Load, in *Wire Ropes: Tension, Endurance, Reliability*, ed. by K. Feyrer, (Springer, Berlin/Heidelberg, 2015a), pp. 59–177
66. K. Feyrer, Wire Ropes, Elements and Definitions, in *Wire Ropes: Tension, Endurance, Reliability*, ed. by K. Feyrer, (Springer, Berlin/Heidelberg, 2015b), pp. 1–57
67. R.B. Figueiredo, F.L. Sicupira, L.R.C. Malheiros, M. Kawasaki, D.B. Santos, T.G. Langdon, Formation of epsilon martensite by high-pressure torsion in a TRIP steel. Mater. Sci. Eng. A **625**, 114–118 (2015)
68. Y. Fukuda, K. Oh-ishi, Z. Horita, T.G. Langdon, Processing of a low-carbon steel by equal-channel angular pressing. Acta Mater. **50**(6), 1359–1368 (2002)
69. M.C. García-Alonso, J.L. González-Carrasco, P. Pérez, V.A.C. Haanappel, M.L. Escudero, J. Chao, M.F. Stroosnijder, A surface modified ODS superalloy by thermal oxidation for potential implant applications. J. Mater. Sci. Mater. Med. **12**(7), 589–596 (2001)
70. C. Garcia-Mateo, TIANOBAIN-towards industrial applicability of (medium C) nanostructured bainitic steels-RFCS. Impact **2018**(1), 94–96 (2018)
71. C. Garcia-Mateo, F.G. Caballero, Ultra-high-strength bainitic steels. ISIJ Int. **45**(11), 1736–1740 (2005)
72. C. Garcia-Mateo, F.G. Caballero, H.K.D.H. Bhadeshia, Development of hard Bainite. ISIJ Int. **43**(8), 1238–1243 (2003a)
73. C. Garcia-Mateo, C. Fg, B. Hkdh, Acceleration of low-temperature bainite. ISIJ Int. **43**(11), 1821–1825 (2003b)
74. C. Garcia-Mateo, M. Peet, F.G. Caballero, H. Bhadeshia, Tempering of hard mixture of bainitic ferrite and austenite. Mater. Sci. Technol. **20**(7), 814–818 (2004)
75. C. Garcia-Mateo, F.G. Caballero, M.K. Miller, J.A. Jimenez, On measurement of carbon content in retained austenite in a nanostructured bainitic steel. J. Mater. Sci. **47**(2), 1004–1010 (2012)
76. C. Garcia-Mateo, T. Sourmail, F.G. Caballero, V. Smanio, M. Kuntz, C. Ziegler, A. Leiro, E. Vuorinen, R. Elvira, T. Teeri, Nanostructured steel industrialisation: Plausible reality. Mater. Sci. Technol. **30**(9), 1071–1078 (2014)
77. C. Garcia-Mateo, J.A. Jimenez, H.W. Yen, M.K. Miller, L. Morales-Rivas, M. Kuntz, S.P. Ringer, J.R. Yang, F.G. Caballero, Low temperature bainitic ferrite: Evidence of carbon supersaturation and tetragonality. Acta Mater. **91**, 162–173 (2015)
78. C. Garcia-Mateo, G. Paul, M.C. Somani, D.A. Porter, L. Bracke, A. Latz, C. Garcia De Andres, F.G. Caballero, Transferring nanoscale Bainite concept to lower C contents: A perspective. Metals **7**(5), 159 (2017)
79. V.G. Gavriljuk, Decomposition of cementite in pearlitic steel due to plastic deformation. Mater. Sci. Eng. A **345**(1–2), 81–89 (2003)
80. G. Ghosh, G.B. Olson, Computational thermodynamics and the kinetics of martensitic transformation. J. Phase Equilibria **22**(3), 199–207 (2001)

81. C. Ghosh, M. Shome, Dynamic strain aging during wire drawing and its effect on electrochemical behaviour. Ironmak. Steelmak. **44**(10), 789–795 (2017)
82. H. Gleiter, Chapter 9: Microstructure, in *Physical Metallurgy*, ed. by R. W. Cahn, P. Haasen, 4th edn., (Oxford, North-Holland, 1996), pp. 843–942
83. H. Gleiter, Nanostructured materials: Basic concepts and microstructure. Acta Mater. **48**(1), 1–29 (2000)
84. H. Gleiter, N. Hansen, A. Horsewell, T. Leffers, H. Lilholt, Deformation of polycrystals: Mechanisms and microstructures
85. W. Gong, Y. Tomota, S. Harjo, Y.H. Su, K. Aizawa, Effect of prior martensite on bainite transformation in nanobainite steel. Acta Mater. **85**, 243–249 (2015)
86. S. Goto, R. Kirchheim, T. Al-Kassab, C. Borchers, Application of cold drawn lamellar microstructure for developing ultra-high strength wires. Trans. Nonfer. Metal Soc. China (English Edition) **17**(6), 1129–1138 (2007)
87. G. Gottstein, L.S. Shvindlerman, Triple junction drag and grain growth in 2D polycrystals. Acta Mater. **50**(4), 703–713 (2002)
88. T. Gräning, M. Rieth, A. Möslang, A. Kuzmin, A. Anspoks, J. Timoshenko, A. Cintins, J. Purans, Investigation of precipitate in an austenitic ODS steel containing a carbon-rich process control agent. Nucl. Mater. Energy **15**, 237–243 (2018)
89. S.L. Grassie, *Mechanics and Fatigue in Wheel/Rail Contact* (Elsevier, 2012)
90. V. Guttmann, A. Mediavilla, O. Ruano, Preoxidized ma 956 in an S-O-C-bearing atmosphere. Mater. High Temp. **11**(1–4), 42–50 (1993)
91. G.A.J. Hack, Developments in the production of oxide dispersion strengthened superalloys. Powder Metall. **27**(2), 73–79 (1984)
92. E.O. Hall, The deformation and ageing of mild steel: III discussion of results. Proc. Phys. Soc. Sect. B **64**(9), 747 (1951)
93. R.G. Hamerton, D.M. Jaeger, A.R. Jones, New enhanced performance stainless steel. Mater. World **1**(1), 9–10 (1993)
94. K. Han, G.D.W. Smith, D.V. Edmonds, Pearlite phase transformation in Si and V steel. Metall. Mater. Trans. A **26**(7), 1617–1631 (1995)
95. H.S. Hasan, M.J. Peet, H.K.D.H. Bhadeshia, Severe tempering of bainite generated at low transformation temperatures. Int. J. Mater. Res. **103**(11), 1319–1324 (2012)
96. H.S. Hasan, M.J. Peet, M.N. Avettand-Fènoël, H.K.D.H. Bhadeshia, Effect of tempering upon the tensile properties of a nanostructured bainitic steel. Mater. Sci. Eng. A **615**, 340–347 (2014)
97. M.F. Hawkes, R.F. Mehl, The effect of cobalt on the rate of nucleation and the rate of growth of pearlite. Trans. Am. Inst. Min. Metall. Petrol. Eng. **172**, 467–492 (1947)
98. R.F. Hehemann, K.R. Kinsman, H.I. Aaronson, A debate on the bainite reaction. Metall. Trans. **3**(5), 1077–1094 (1972)
99. J. Henry, S.A. Maloy, *9 - Irradiation-Resistant Ferritic and Martensitic Steels as Core Materials for Generation IV Nuclear Reactors. Structural Materials for Generation IV Nuclear Reactors. P. Yvon* (Woodhead Publishing, 2017), pp. 329–355
100. I. Hilger, M. Tegel, M.J. Gorley, P.S. Grant, T. Weißgärber, B. Kieback, The structural changes of Y2O3 in ferritic ODS alloys during milling. J. Nucl. Mater. **447**(1–3), 242–247 (2014)
101. C.E. Hinchliffe, G.D.W. Smith, Strain aging of pearlitic steel wire during post-drawing heat treatments. Mater. Sci. Technol. **17**(2), 148–154 (2001)
102. D. T. Hoelzer, J. Bentley, M. K. Miller, M. K. Sokolov, T. S. Byun, M. Li, Development of High-Strength ODS Steels for Nuclear Energy Applications. ODS 2010 Materials Workshop. ODS 2010 Materials Workshop, Qualcomm Conference Center Jacobs Hall, University of California, San Diego (2010)
103. M.H. Hong, K. Hono, W.T. Reynolds, T. Tarui, Atom probe and transmission electron microscopy investigations of heavily drawn pearlitic steel wire. Metall. Mater. Trans. A **30**(3), 717–727 (1999)
104. M. Honjo, T. Kimura, K. Hase, Effect of Cr on lamellar spacing and high-temperature stability in eutectoid steels. ISIJ Int. **56**(1), 161–167 (2016)

105. K. Hono, M. Ohnuma, M. Murayama, S. Nishida, A. Yoshie, T. Takahashi, Cementite decomposition in heavily drawn pearlite steel wire. Scr. Mater. **44**(6), 977–983 (2001)
106. P. Hosemann, H.T. Thau, A.L. Johnson, S.A. Maloy, N. Li, Corrosion of ODS steels in lead–bismuth eutectic. J. Nucl. Mater. **373**(1), 246–253 (2008)
107. C.X. Huang, G. Yang, B. Deng, S.D. Wu, S.X. Li, Z.F. Zhang, Formation mechanism of nanostructures in austenitic stainless steel during equal channel angular pressing. Philos. Mag. **87**(31), 4949–4971 (2007)
108. C.N. Hulme-Smith, I. Lonardelli, A.C. Dippel, H.K.D.H. Bhadeshia, Experimental evidence for non-cubic bainitic ferrite. Scr. Mater. **69**(5), 409–412 (2013)
109. Y.-M. Hwang, T.-Y. Kuo, Dieless drawing of stainless steel tubes. Int. J. Adv. Manuf. Technol. **68**(5), 1311–1316 (2013)
110. A. Inoue, T. Ogura, T. Masumoto, Burgers vectors of dislocations in cementite crystal. Scr. Metall. **11**(1), 1–5 (1977)
111. Y.V. Ivanisenko, W. Lojkowski, R.Z. Valiev, H.J. Fecht, The strain induced cementite dissolution in carbon steel - experimental facts and theoretical approach. Solid State Phenom. **94**, 45–50 (2003)
112. Y.S. Jang, M.P. Phaniraj, D.-I. Kim, J.-H. Shim, M.-Y. Huh, Effect of Aluminum content on the microstructure and mechanical properties of hypereutectoid steels. Metall. Mater. Trans. A **41**(8), 2078–2084 (2010)
113. A.R. Jones, J. Ritherdon, Reduction in defect content of oxide dispersion strengthened alloys. Mater. High Temp. **16**(4), 181–188 (1999)
114. C.P. Jongenburger, R.F. Singer, *Recrystallization of Ods Superalloys* (Dgm Metallurgy Information, New York, 1989)
115. D. Juul Jensen, Growth rates and misorientation relationships between growing nuclei/grains and the surrounding deformed matrix during recrystallization. Acta Metall. Mater. **43**(11), 4117–4129 (1995)
116. R. Kapoor, *Severe Plastic Deformation of Materials. Materials Under Extreme Conditions* (Elsevier, 2017), pp. 717–754
117. L. Kaufman, M. Cohen, Thermodynamics and kinetics of martensitic transformations. Prog. Met. Phys. **7**, 165–246 (1958)
118. B. Kazimierzak, J.M. Prignon, R.I. Fromont, An ODS material with outstanding creep and oxidation resistance above 1100°C. Mater. Des. **13**(2), 67–70 (1992)
119. K. Kempen, E. Yasa, L. Thijs, J.P. Kruth, J. Van Humbeeck, Microstructure and mechanical properties of selective laser melted 18Ni-300 steel. Phys. Procedia **12**, 255–263 (2011)
120. J.H. Kim, T.S. Byun, D.T. Hoelzer, C.H. Park, J.T. Yeom, J.K. Hong, Temperature dependence of strengthening mechanisms in the nanostructured ferritic alloy 14YWT: Part II—Mechanistic models and predictions. Mater. Sci. Eng. A **559**, 111–118 (2013)
121. R.L. Klueh, J.P. Shingledecker, R.W. Swindeman, D.T. Hoelzer, Oxide dispersion-strengthened steels: A comparison of some commercial and experimental alloys. J. Nucl. Mater. **341**(2), 103–114 (2005)
122. G. Korb, M. Rühle, H.P. Martinz, *New Iron-Based ODS-Superalloys for High Demanding Applications* (International Gas Turbine and Aeroengine Congress and Exposition, American Society of Mechanical Engineers Digital Collection, 1991)
123. Kourbatoff, Contribution à l'étude métallographique des aciers trempés. Rev. Met. Paris **2**(1), 169–186 (1905)
124. Kourbatoff, Contribution à l'étude métallographique des aciers trempés(1). Rev. Met. Paris **5**(10), 704–710 (1908)
125. E. Kozeschnik, H.K.D.H. Bhadeshia, Influence of silicon on cementite precipitation in steels. Mater. Sci. Technol. **24**(3), 343–347 (2008)
126. G. Krauss, High-carbon steels: Fully pearlitic microstructures and applications. Steels Process. Struct. Perform., 281–295 (2005)
127. L.P. Kubin, Y. Estrin, C. Perrier, On static strain ageing. Acta Metall. Mater. **40**(5), 1037–1044 (1992)

128. P. Kürnsteiner, M.B. Wilms, A. Weisheit, P. Barriobero-Vila, E.A. Jägle, D. Raabe, Massive nanoprecipitation in an Fe-19Ni-xAl maraging steel triggered by the intrinsic heat treatment during laser metal deposition. Acta Mater. **129**, 52–60 (2017)
129. G. Langford, M. Cohen, Calculation of cell-size strengthening of wire-drawn iron. Metall. Mater. Trans. B **1**(5), 1478–1480 (1970)
130. J. Languillaume, G. Kapelski, B. Baudelet, Cementite dissolution in heavily cold drawn pearlitic steel wires. Acta Mater. **45**(3), 1201–1212 (1997)
131. A. Leiro, E. Vuorinen, K.G. Sundin, B. Prakash, T. Sourmail, V. Smanio, F.G. Caballero, C. Garcia-Mateo, R. Elvira, Wear of nano-structured carbide-free bainitic steels under dry rolling–sliding conditions. Wear **298-299**, 42–47 (2013)
132. B. Leng, S. Ukai, Y. Sugino, Q. Tang, T. Narita, S. Hayashi, F. Wan, S. Ohtsuka, T. Kaito, Recrystallization texture of cold-rolled oxide dispersion strengthened Ferritic steel. ISIJ Int. **51**(6), 951–957 (2011)
133. B. Leng, S. Ukai, T. Narita, Y. Sugino, Q. Tang, N. Oono, S. Hayashi, F. Wan, S. Ohtsuka, T. Kaito, Effects of two-step cold rolling on recrystallization Behaviors in ODS Ferritic steel. Mater. Trans. **53**(4), 652–657 (2012)
134. R. Lewis, U. Olofsson, *Wheel-Rail Interface Handbook* (Elsevier, 2009)
135. Y.J. Li, P. Choi, S. Goto, C. Borchers, D. Raabe, R. Kirchheim, Evolution of strength and microstructure during annealing of heavily cold-drawn 6.3GPa hypereutectoid pearlitic steel wire. Acta Mater. **60**(9), 4005–4016 (2012)
136. Y. Li, D. Raabe, M. Herbig, P.-P. Choi, S. Goto, A. Kostka, H. Yarita, C. Borchers, R. Kirchheim, Segregation stabilizes Nanocrystalline bulk steel with near theoretical strength. Phys. Rev. Lett. **113**(10), 106104 (2014)
137. S. Liu, F. Zhang, Z. Yang, M. Wang, C. Zheng, Effects of Al and Mn on the formation and properties of nanostructured pearlite in high-carbon steels. Mater. Des. **93**, 73–80 (2016)
138. L. Liu, Q. Ding, Y. Zhong, J. Zou, J. Wu, Y.-L. Chiu, J. Li, Z. Zhang, Q. Yu, Z. Shen, Dislocation network in additive manufactured steel breaks strength–ductility trade-off. Mater. Today **21**(4), 354–361 (2018a)
139. N. Liu, X. Zhang, J. Ding, J. He, F.-x. Yin, Microstructure and mechanical properties of nanobainitic steel subjected to multiple isothermal heat treatments. J. Iron Steel Res. Int. (2018b)
140. A.J. London, S. Lozano-Perez, M.P. Moody, S. Amirthapandian, B.K. Panigrahi, C.S. Sundar, C.R.M. Grovenor, Quantification of oxide particle composition in model oxide dispersion strengthened steel alloys. Ultramicroscopy **159**, 360–367 (2015)
141. R. Łyszkowski, T. Czujko, R.A. Varin, Multi-axial forging of Fe3Al-base intermetallic alloy and its mechanical properties. J. Mater. Sci. **52**(5), 2902–2914 (2017)
142. E. Ma, T. Zhu, Towards strength–ductility synergy through the design of heterogeneous nanostructures in metals. Mater. Today **20**(6), 323–331 (2017)
143. C. Mack, M.S. Bartlett, *On Clumps Formed When Convex Laminae or Bodies Are Placed at Random in Two or Three Dimensions* (Cambridge University Press, 1956)
144. T.R. Malow, C.C. Koch, Grain growth in nanocrystalline iron prepared by mechanical attrition. Acta Mater. **45**(5), 2177–2186 (1997)
145. S. A. Maloy, E. Aydogan, O. Anderoglu, C. Lavender, I. Anderson, J. Rieken, J. Lewandowski, D. Hoelzer, G. R. Odette, Characterization of Tubing from Advanced ODS alloy (FCRD-NFA1), Los Alamos National Lab.(LANL), Los Alamos, NM (United States); Pacific Northwest National Lab.(PNNL), Richland, WA (United States); Ames Lab., Ames, IA (United States); Oak Ridge National Lab.(ORNL), Oak Ridge, TN (United States) (2016)
146. X. Mao, S.H. Kang, T.K. Kim, S.C. Kim, K.H. Oh, J. Jang, Microstructure and mechanical properties of ultrafine-grained austenitic oxide dispersion strengthened steel. Metall. Mater. Trans. A Phys. Metall. Mater. Sci. **47**(11), 5334–5343 (2016)
147. L. Marechal, B. Lesage, A.M. Huntz, R. Molins, Oxidation behavior of ODS Fe-Cr-Al alloys: Aluminum depletion and lifetime. Oxid. Met. **60**(1–2), 1–28 (2003)
148. N. Maruyama, T. Tarui, H. Tashiro, Atom probe study on the ductility of drawn pearlitic steels. Scr. Mater. **46**(8), 599–603 (2002)

149. S.J. Matas, R.F. Hehemann, The structure of bainite in hypoeutectoid steels. Trans. Metall. Soc. AIME **221**(1), 179–185 (1961)
150. R.F. Mehl, The structure and rate of formation of pearlite. Trans. Am. Soc. Metal. **29**(4), 813–862 (1941)
151. R.F. Mehl, The structure and rate of formation of pearlite. Metall. Microstruct. Analy. **4**(5), 423–443 (2015)
152. G. Merceron, R. Molins, J.L. Strudel, Oxidation behaviour and microstructural evolution of FeCrAI ODS alloys at high temperature. 4th Int. Conf. Micros. Oxid. **17**(1), 149–157 (2000)
153. M.K. Miller, C.M. Parish, Role of alloying elements in nanostructured ferritic steels. Mater. Sci. Technol. **27**(4), 729–734 (2011)
154. M.K. Miller, C.M. Parish, Q. Li, *Advanced Oxide Dispersion Strengthened and Nanostructured Ferritic Alloys* (Taylor & Francis, 2013a)
155. M.K. Miller, C.M. Parish, Q. Li, Advanced oxide dispersion strengthened and nanostructured ferritic alloys. Mater. Sci. Technol. **29**(10), 1174–1178 (2013b)
156. N. Min, W. Li, X. Jin, X. Wang, T. Yang, C. Zhang, Influence of aging on the mechanical property of a cold drawn pearlite steel. Jinshu Xuebao/Acta Metallurgica Sinica **42**(10), 1009–1013 (2006)
157. N. Min, W. Li, H. Li, X. Jin, Atom probe and mössbauer spectroscopy investigations of cementite dissolution in a cold drawn eutectoid steel. J. Mater. Sci. Technol. **26**(9), 776–782 (2010)
158. Y. Mine, D. Haraguchi, Z. Horita, K. Takashima, High-pressure torsion of metastable austenitic stainless steel at moderate temperatures. Philos. Mag. Lett. **95**(5), 269–276 (2015)
159. L. Morales-Rivas, *Microstructure and Mechanical Response of Nanostructured Bainitic Steels* (Universidad Carlos III de Madrid, 2016)
160. L. Morales-Rivas, A. González-Orive, C. Garcia-Mateo, A. Hernández-Creus, F.G. Caballero, L. Vázquez, Nanomechanical characterization of nanostructured bainitic steel: Peak force microscopy and Nanoindentation with AFM. Sci. Rep. **5**, 17164 (2015)
161. L. Morales-Rivas, C. Garcia-Mateo, T. Sourmail, M. Kuntz, R. Rementeria, F.G. Caballero, Ductility of nanostructured bainite. Metals **6**(12), 302 (2016)
162. L. Morales-Rivas, F. Archie, S. Zaefferer, M. Benito-Alfonso, S.-P. Tsai, J.-R. Yang, D. Raabe, C. Garcia-Mateo, F.G. Caballero, Crystallographic examination of the interaction between texture evolution, mechanically induced martensitic transformation and twinning in nanostructured bainite. J. Alloys Compd. **752**, 505–519 (2018)
163. S. Morito, H. Yoshida, T. Maki, X. Huang, Effect of block size on the strength of lath martensite in low carbon steels. Mater. Sci. Eng. A **438-440**, 237–240 (2006)
164. I. Mueller, R. Rementeria, F.G. Caballero, M. Kuntz, T. Sourmail, E. Kerscher, A constitutive relationship between fatigue limit and microstructure in nanostructured bainitic steels. Materials **9**(10), 831 (2016)
165. K. Murakami, K. Mino, H. Harada, H. Bhadeshia, Nonuniform recrystallization in a mechanically alloyed nickel-base superalloy. Metall. Trans.Phys. Metall. Mater. Sci. **24**(5), 1049–1055 (1993)
166. W.J. Nam, C.M. Bae, Void initiation and microstructural changes during wire drawing of pearlitic steels. Mater. Sci. Eng. A **203**(1–2), 278–285 (1995)
167. W.J. Nam, H.R. Song, C.M. Bae, Effect of microstructural features on ductility of drawn Pearlitic carbon steels. ISIJ Int. **45**(8), 1205–1210 (2005)
168. T. Narita, S. Ukai, B. Leng, S. Ohtsuka, T. Kaito, Characterization of recrystallization of 12Cr and 15Cr ODS ferritic steels. J. Nucl. Sci. Technol. **50**(3), 314–320 (2013)
169. J.P. Naylor, The influence of the lath morphology on the yield stress and transition temperature of martensitic- bainitic steels. Metall. Trans. A. **10**(7), 861–873 (1979)
170. A. Nordmann, Invisible origins of nanotechnology: Herbert Gleiter, materials science, and questions of prestige. Perspect. Sci. **17**(2), 123–143 (2009)
171. I. Ochiai, S. Nishida, H. Ohba, A. Kawana, Application of hypereutectoid steel for development of high strength steel wire. Tetsu-to-Hagane **79**(9), 1101–1107 (1993)

172. I. Ochial, Effect of metallurgical factors on strengthening of steel tire cord. Wire J. Int. (USA) **26**(12), 50–61 (1993)
173. G.R. Odette, Recent Progress in developing and qualifying nanostructured Ferritic alloys for advanced fission and fusion applications. JOM **66**(12), 2427–2441 (2014)
174. G.R. Odette, On the status and prospects for nanostructured ferritic alloys for nuclear fission and fusion application with emphasis on the underlying science. Scr. Mater. **143**, 142–148 (2018)
175. G.R. Odette, M.J. Alinger, B.D. Wirth, Recent developments in irradiation-resistant steels. Annu. Rev. Mater. Res. **38**, 471–503 (2008)
176. H. Ohba, S. Nishida, T. Tarui, K. Yoshimua, M. Sugimoto, K. Matsuoka, N. Hikita, M. Toda, High-performance wire rods produced with DLP. Nippon Steel Tech. Rep. **96**(6), 50–56 (2007)
177. H. Oka, T. Tanno, S. Ohtsuka, Y. Yano, T. Kaito, Effect of nitrogen concentration on nanostructure and high-temperature strength of 9Cr-ODS steel. Nucl. Mater. Ener. **16**, 230–237 (2018)
178. A.K. Padap, G.P. Chaudhari, V. Pancholi, S.K. Nath, Warm multiaxial forging of AISI 1016 steel. Mater. Des. **31**(8), 3816–3824 (2010)
179. S. Pal, M.E. Alam, G.R. Odette, J. Lewandowski, D.T. Hoelzer, S.A. Maloy, Characterization of microstructure and texture of NFA-1 for two deformation-processing routes. Fusion Mater. Semiannu. Prog. Rep. **58**, 29–41 (2015)
180. A. S. Pandit, Theory of the pearlite transformation in steels (2011)
181. H.G. Paris, D.K. Kim, Metallurgy, processing and applications of metal wires. TMS (1996)
182. D.B. Park, J.W. Lee, Y.S. Lee, K.T. Park, W.J. Nam, Effects of the annealing temperature and time on the microstructural evolution and corresponding the mechanical properties of cold-drawn steel wires. Met. Mater. Int. **14**(1), 59–64 (2008)
183. M.J. Peet, S.S. Babu, M.K. Miller, H. Bhadeshia, Tempering of low-temperature bainite. Metall. Mater. Trans. A **48**(7), 3410–3418 (2017)
184. G.E. Pellisier, M.F. Hawkes, W.A. Johnson, R.F. Mehl, The interlamellar spacing of pearlite. Trans. Am. Soc. Metal. **30**, 1049–1086 (1942)
185. J.J. Pepe, Deformation structure and the tensile fracture characteristics of a cold worked 1080 pearlitic steel. Metall. Trans. **4**(10), 2455–2460 (1973)
186. E.V. Pereloma, Critical assessment 20: On carbon excess in bainitic ferrite. Mater. Sci. Technol. **32**(2), 99–103 (2016)
187. A.J. Perez-Unzueta, J.H. Beynon, Microstructure and wear resistance of pearlitic rail steels. Wear **162**, 173–182 (1993)
188. N.J. Petch, The cleavage strength of polycrystals. J. Iron Steel Inst. **174**, 25–28 (1953)
189. G. Pimentel, J. Chao, C. Capdevila, Recrystallization process in Fe-Cr-Al oxide dispersion-strengthened alloy: Microstructural evolution and recrystallization mechanism. JOM **66**(5), 780–792 (2014)
190. J.-P. Poirier, The Coming of Materials Science. R.W. Cahn. Pergamon, 2001 (568 pages). 130 NL guilders, hardback, ISBN 0-08-042679-4." Eur. Rev. 9(4): 517–522 (2001)
191. M. Praud, F. Mompiou, J. Malaplate, D. Caillard, J. Garnier, A. Steckmeyer, B. Fournier, Study of the deformation mechanisms in a Fe–14% Cr ODS alloy. J. Nucl. Mater. **428**(1), 90–97 (2012)
192. J. Pujante, D. Casellas, T. Sourmail, F. G. Caballero, A. Soto, J. M. Llanos, E. Vuorinen, B. Prakash, J. Hardell, P. V. Moghaddam, Novel Nano-structured Bainitic steels for enhanced durability of Wear resistant components: Microstructural optimisation through simulative Wear and field tests, BAINWEAR (2018)
193. M.P. Puls, J.S. Kirkaldy, The pearlite reaction. Metall. Trans. **3**(11), 2777–2796 (1972)
194. K.G. Raghavendra, A. Dasgupta, C. Ghosh, K. Jayasankar, V. Srihari, S. Saroja, Development of a novel ZrO2 dispersion strengthened 9Cr ferritic steel: Characterization of milled powder and subsequent annealing behavior. Powder Technol. **327**, 267–274 (2018)
195. H. Regle, A. Alamo, Secondary recrystallization of oxide dispersion strengthened ferritic alloys. Journal De Physique, Paris, Fr, Publ by Editions de Physique (1993)

196. M. Reibold, P. Paufler, A.A. Levin, W. Kochmann, N. Pätzke, D.C. Meyer, Materials: Carbon nanotubes in an ancient Damascus sabre. Nature **444**(7117), 286 (2006)
197. R. Rementeria, L. Morales-Rivas, M. Kuntz, C. Garcia-Mateo, E. Kerscher, T. Sourmail, F.G. Caballero, On the role of microstructure in governing the fatigue behaviour of nanostructured bainitic steels. Mater. Sci. Eng. A **630**, 71–77 (2015)
198. R. Rementeria, M.M. Aranda, C. Garcia-Mateo, F.G. Caballero, Improving wear resistance of steels through nanocrystalline structures obtained by bainitic transformation. Mater. Sci. Technol. **32**(4), 308–312 (2016)
199. R. Rementeria, J.A. Jimenez, S.Y.P. Allain, G. Geandier, J.D. Poplawsky, W. Guo, E. Urones-Garrote, C. Garcia-Mateo, F.G. Caballero, Quantitative assessment of carbon allocation anomalies in low temperature bainite. Acta Mater. **133**, 333–345 (2017a)
200. R. Rementeria, J.D. Poplawsky, M.M. Aranda, W. Guo, J.A. Jimenez, C. Garcia-Mateo, F.G. Caballero, Carbon concentration measurements by atom probe tomography in the ferritic phase of high-silicon steels. Acta Mater. **125**, 359–368 (2017b)
201. R. Rementeria, C. Garcia-Mateo, F.G. Caballero, New insights into carbon distribution in Bainitic ferrite. HTM J. Heat Treat. Mater. **73**(2), 68–79 (2018)
202. S.O. Rogachev, V.M. Khatkevich, R.O. Kaibyshev, M.S. Tikhonova, S.V. Dobatkin, Nitrided 08Kh17T steel after high-pressure torsion. Russ. Metall. (Metally) **2015**(11), 861–867 (2015)
203. J. Rösler, E. Arzt, A new model-based creep equation for dispersion strengthened materials. Acta Metall. Mater. **38**(4), 671–683 (1990)
204. D. A. Rutherford, R. J. McWilliams, Surface Hardening of Rails, Google Patents (1970)
205. K. Saeki, K. Iwano, Progress and prospects of rail for railroads. Nippon Steel Sumitomo Met. Tech. Rep. **105**, 19–25 (2013)
206. N. Sallez, C. Hatzoglou, F. Delabrouille, D. Sornin, L. Chaffron, M. Blat-Yrieix, B. Radiguet, P. Pareige, P. Donnadieu, Y. Bréchet, Precipitates and boundaries interaction in ferritic ODS steels. J. Nucl. Mater. **472**, 118–126 (2016)
207. B.P.J. Sandvik, The bainite reaction in Fe– Si– C alloys: The primary stage. Metall. Trans. A. **13**(5), 777–787 (1982a)
208. B.P.J. Sandvik, The Bainite reaction in Fe– Si– C alloys: The secondary stage. Metall. Trans. A. **13**(5), 789–800 (1982b)
209. M.A. Santajuana, R. Rementeria, M. Kuntz, J.A. Jimenez, F.G. Caballero, C. Garcia-Mateo, Low-temperature Bainite: A thermal stability study. Metall. Mater. Trans. A **49**(6), 2026–2036 (2018)
210. S. Sato, K. Wagatsuma, S. Suzuki, M. Kumagai, M. Imafuku, H. Tashiro, K. Kajiwara, T. Shobu, Relationship between dislocations and residual stresses in cold-drawn pearlitic steel analyzed by energy-dispersive X-ray diffraction. Mater. Charact. **83**, 152–160 (2013)
211. X. Sauvage, J. Copreaux, F. Danoix, D. Blavette, Atomic-scale observation and modelling of cementite dissolution in heavily deformed pearlitic steels. Philos. Mag. A Phys. Cond. Matt. Struct. Defect. Mech. Prop. **80**(4), 781–796 (2000)
212. J.H. Schneibel, M. Heilmaier, Hall-Petch breakdown at elevated temperatures. Mater. Trans. **55**(1), 44–51 (2014)
213. K. Schwab, *The Fourth Industrial Revolution* (Crown Business, 2017)
214. J.G. Sevillano, Room temperature plastic deformation of pearlitic cementite. Mater. Sci. Eng. **21**(C), 221–225 (1975)
215. C.W. Shao, P. Zhang, Y.K. Zhu, Z.J. Zhang, Y.Z. Tian, Z.F. Zhang, Simultaneous improvement of strength and plasticity: Additional work-hardening from gradient microstructure. Acta Mater. **145**, 413–428 (2018)
216. J. Shen, H. Yang, Z. Zhao, J. McGrady, S. Kano, H. Abe, Effects of pre-deformation on microstructural evolution of 12Cr ODS steel under 1473–1673 K annealing. Nucl. Mater. Ener **16**, 137–144 (2018)
217. A. Shirzadi, S. Jackson, *Structural Alloys for Power Plants: Operational Challenges and High-temperature Materials* (Elsevier, 2014)
218. C.T. Sims, N.S. Stoloff, W.C. Hagel, *Superalloys II* (Wiley, 1987)

219. R.F. Singer, G.H. Gessinger, Hot isostatic pressing of oxide dispersion strengthened superalloy parts. Powder Metall. Int. **15**(3), 119–121 (1983)
220. S.B. Singh, H.K.D.H. Bhadeshia, Estimation of bainite plate-thickness in low-alloy steels. Mater. Sci. Eng. A **245**(1), 72–79 (1998)
221. C.S. Smith, *A History of Metallography: The Development of Ideas on the Structure of Metals before 1890* (University of Chicago Press, Chicago, 1960)
222. R.A. Smith, Fatigue in transport: Problems, solutions and future threats. Process Saf. Environ. Prot. **76**(3), 217–223 (1998)
223. M.A. Sokolov, D.T. Hoelzer, R.E. Stoller, D.A. McClintock, Fracture toughness and tensile properties of nano-structured ferritic steel 12YWT. J. Nucl. Mater. **367-370**, 213–216 (2007)
224. B. Song, X. Zhao, S. Li, C. Han, Q. Wei, S. Wen, J. Liu, Y. Shi, Differences in microstructure and properties between selective laser melting and traditional manufacturing for fabrication of metal parts: A review. Front. Mech. Eng. **10**(2), 111–125 (2015)
225. T. Sourmail, Bainite and Superbainite in long products and forged applications. HTM J. Heat Treat. Mat. **72**(6), 371–378 (2017)
226. T. Sourmail, V. Smanio, Low temperature kinetics of bainite formation in high carbon steels. Acta Mater. **61**(7), 2639–2648 (2013)
227. T. Sourmail, F.G. Caballero, C. Garcia-Mateo, V. Smanio, C. Ziegler, M. Kuntz, R. Elvira, A. Leiro, E. Vuorinen, T. Teeri, Evaluation of potential of high Si high C steel nanostructured bainite for wear and fatigue applications. Mater. Sci. Technol. **29**(10), 1166–1173 (2013a)
228. T. Sourmail, V. Smanio, C. Ziegler, V. Heuer, M. Kuntz, F.G. Caballero, C. Garcia-Mateo, J. Cornide, R. Elvira, A. Leiro, *Novel Nanostructured Bainitic Steel Grades to Answer the Need for High-Performance Steel Components (Nanobain)* (D.-G. f. R. a. I. D. G. I. T. U. G. R. F. f. C. a. Steel, Brussels, European Comission, 2013b)
229. T. Sourmail, F. Danoix, C. Garcia-Mateo, F.G. Caballero, R. Rementeria, L. Morales-Rivas, R. Pizzaro, R. Janisch, S. Sampath, I. Mueller, E. Kerscher, M. Kuntz, *Understanding Basic Mechanism to Optimize and Predict in Service Properties of Nanobainitic Steels (MECBAIN)* (E. C. D.-G. f. R. a. I. D. D. I. T. U. D. C. a. Steel, Brussels, European Comission, 2017a)
230. T. Sourmail, C. Garcia-Mateo, F.G. Caballero, L. Morales-Rivas, R. Rementeria, M. Kuntz, Tensile ductility of nanostructured bainitic steels: Influence of retained austenite stability. Metals **7**(1), 31 (2017b)
231. D. Sporer, K. Lempenauer, PM ODS materials for high temperature applications, in *13th International Plansee Seminars*, (Freund Publ. House, Reutte, Austria, 1994)
232. T. S. Srivatsan, C. Daniels, A. Prakash, High cycle fatigue behavior of high carbon steel wires. Proceedings of the Annual Convention of the Wire Association International (1997)
233. D. H. Stone, G. G. Knupp, T. American Society for, S. S. Materials. Committee A-1 on Steel and A. Related, Rail steels, developments, processing, and use: a symposium sponsored by ASTM Committee A-1 on Steel, Stainless Steel, and Related Alloys, American Society for Testing and Materials, Denver, Colo., 17–18 Nov. 1976, American Society for Testing and Materials (1978)
234. D. Strong, I. Sirichakwal, G.P. Manogharan, T. Wakefield, Current state and potential of additive–hybrid manufacturing for metal parts. Rapid Prototyp. J. **23**(3), 577–588 (2017)
235. K. Suresh, M. Nagini, R. Vijay, M. Ramakrishna, R.C. Gundakaram, A.V. Reddy, G. Sundararajan, Microstructural studies of oxide dispersion strengthened austenitic steels. Mater. Des. **110**, 519–525 (2016)
236. P.J. Szabó, P. Bereczki, B. Verő, The effect of multiaxial forging on the grain refinement of low alloyed steel. Period. Polytech. Mech. Eng. **55**(1), 63–66 (2011)
237. T. Takahashi, M. Nagumo, Flow stress and work-hardening of Pearlitic steel. Trans. Jpn. Inst. Metals **11**(2), 113–119 (1970)
238. J. Takahashi, T. Tarui, K. Kawakami, Three-dimensional atom probe analysis of heavily drawn steel wires by probing perpendicular to the pearlitic lamellae. Ultramicroscopy **109**(2), 193–199 (2009)
239. J. Takahashi, M. Kosaka, K. Kawakami, T. Tarui, Change in carbon state by low-temperature aging in heavily drawn pearlitic steel wires. Acta Mater. **60**(1), 387–395 (2012)

240. E.M. Taleff, J.J. Lewandowski, B. Pourladian, Microstructure-property relationships in pearlitic eutectoid and hypereutectoid carbon steels. JOM **54**(7), 25–30 (2002)
241. T. Tarui, N. Maruyama, J. Takahashi, S. Nishida, H. Tashiro, Microstructure control and strengthening of high-carbon steel wires. Nippon Steel Tech. Rep **91**, 56–61 (2005)
242. H. Tashiro, H. Sato, Effect of alloying elements on the lamellar spacing and the degree of regularity of pearlite in eutectoid steel. J. Jpn. Inst. Metals **55**(10), 1078–1085 (1991)
243. G.F. Taylor, A method of drawing metallic filaments and a discussion of their properties and uses. Phys. Rev. **23**(5), 655 (1924)
244. K.A. Taylor, M. Cohen, Aging of ferrous martensites. Prog. Mater. Sci. **36**, 151–272 (1992)
245. M. Tikhonova, R. Kaibyshev, X. Fang, W. Wang, A. Belyakov, Grain boundary assembles developed in an austenitic stainless steel during large strain warm working. Mater. Charact. **70**, 14–20 (2012)
246. I.B. Timokhina, H. Beladi, X.Y. Xiong, Y. Adachi, P.D. Hodgson, Nanoscale microstructural characterization of a nanobainitic steel. Acta Mater. **59**(14), 5511–5522 (2011)
247. I.B. Timokhina, K.-D. Liss, D. Raabe, K. Rakha, H. Beladi, X.Y. Xiong, P.D. Hodgson, Growth of bainitic ferrite and carbon partitioning during the early stages of bainite transformation in a 2 mass% silicon steel studied by in situ neutron diffraction, TEM and APT. J. Appl. Crystallogr. **49**(2), 399–414 (2016)
248. J. Toribio, E. Ovejero, Effect of cumulative cold drawing on the pearlite interlamellar spacing in eutectoid steel. Scr. Mater. **39**(3), 323–328 (1998)
249. N. Tsuji, Y. Saito, H. Utsunomiya, S. Tanigawa, Ultra-fine grained bulk steel produced by accumulative roll-bonding (ARB) process. Scr. Mater. **40**(7), 795–800 (1999)
250. S. Ukai, M. Harada, H. Okada, M. Inoue, S. Nomura, S. Shikakura, K. Asabe, T. Nishida, M. Fujiwara, Alloying design of oxide dispersion strengthened ferritic steel for long life FBRs core materials. J. Nucl. Mater. **204**, 65–73 (1993)
251. S. Ukai, T. Okuda, M. Fujiwara, T. Kobayashi, S. Mizuta, H. Nakashima, Characterization of high temperature creep properties in recrystallized 12Cr-ODS ferritic steel claddings. J. Nucl. Sci. Technol. **39**(8), 872–879 (2002)
252. S. Ukai, R. Miyata, S. Kasai, N. Oono, S. Hayashi, T. Azuma, R. Kayano, E. Maeda, S. Ohtsuka, Super high-temperature strength in hot rolled steels dispersing nanosized oxide particles. Mater. Lett. **209**, 581–584 (2017)
253. E.E. Underwood, *The Mathematical Foundations of Quantitative Stereology. Stereology and Quantitative Metallography* (ASTM International, 1972)
254. R.Z. Valiev, R.K. Islamgaliev, I.V. Alexandrov, Bulk nanostructured materials from severe plastic deformation. Prog. Mater. Sci. **45**(2), 103–189 (2000)
255. R. Z. Valiev, A. P. Zhilyaev, T. G. Langdon, Bulk Nanostructured Materials: Fundamentals and Applications, Wiley (2013)
256. G.F. Vander Voort, The Interlamellar spacing of pearlite. Prac. Metall. **52**(8), 419–436 (2015)
257. G.F. Vander Voort, A. Roósz, Measurement of the interlamellar spacing of pearlite. Metallography **17**(1), 1–17 (1984)
258. J.D. Verhoeven, A.H. Pendray, W.E. Dauksch, S.R. Wagstaff, Damascus steel revisited. JOM **70**(7), 1331–1336 (2018)
259. R. Verreet, What we Can Learn from Wire Rope Failures: Predictable and Unpredictable Rope Failures. Safe Use of Ropes: Proceedings of the OIPEEC Conference 2011. College Station, Texas (2011)
260. R. Verret, W. Lindsey, Wire rope inspection and examination. Aachen, PR GmbH Werbeagentur und Verlag: 31 (1996)
261. M. Wang, J. Shan, C. Zheng, M. Zhang, Z. Yang, F. Zhang, Effects of deformation and addition of aluminium on spheroidisation of high-carbon-bearing steel. Mater. Sci. Technol. **34**(2), 161–171 (2018)
262. G.S. Was, *Irradiation Hardening and Deformation. Fundamentals of Radiation Materials Science: Metals and Alloys. G. S. Was* (Springer, Berlin/Heidelberg, 2007), pp. 581–642
263. P. Watté, J. Van Humbeeck, E. Aernoudt, I. Lefever, Strain ageing in heavily drawn eutectoid steel wires. Scr. Mater. **34**(1), 89–95 (1996)

264. M. K. West, Processing and characterization of oxide dispersion strengthened 14YWT ferritic alloys. PhD, University of Tennessee (2006)
265. S. Westerkamp, Electrical Resistance, Critical Shear Strength, and Microstructure of Pearlitic Steel Cold Drawn to Varying Degrees of Deformation (2010)
266. S.H. Whang, *Nanostructured Metals and Alloys: Processing, Microstructure, Mechanical Properties and Applications* (Elsevier, 2011)
267. J.D. Whittenberger, Effect of strain rate on the fracture behavior at 1366 K of the bcc iron base oxide dispersion strengthened alloy MA 956. Metall. Trans. A. **10**(9), 1285–1295 (1979)
268. C.A. Williams, P. Unifantowicz, N. Baluc, G.D.W. Smith, E.A. Marquis, The formation and evolution of oxide particles in oxide-dispersion-strengthened ferritic steels during processing. Acta Mater. **61**(6), 2219–2235 (2013)
269. E.A. Wilson, The $\gamma \rightarrow \alpha$ transformation in iron and its dilute alloys. Scr. Metall. **4**(4), 309–311 (1970)
270. R.N. Wright, *Wire Technology: Process Engineering and Metallurgy* (Butterworth-Heinemann, 2016)
271. K.M. Wu, H.K.D.H. Bhadeshia, Extremely fine pearlite by continuous cooling transformation. Scr. Mater. **67**(1), 53–56 (2012)
272. Y. Wu, E.M. Haney, N.J. Cunningham, G.R. Odette, Transmission electron microscopy characterization of the nanofeatures in nanostructured ferritic alloy MA957. Acta Mater. **60**(8), 3456–3468 (2012)
273. Y. Wu, J. Ciston, S. Kräemer, N. Bailey, G.R. Odette, P. Hosemann, The crystal structure, orientation relationships and interfaces of the nanoscale oxides in nanostructured ferritic alloys. Acta Mater. **111**, 108–115 (2016)
274. Y. Wu, T. Stan, J. Ciston, G. R. Odette, DOE Fusion Materials Semiannual Progress Report, DOE/ER-0313/61 (2017)
275. S. Yamashita, S. Ohtsuka, N. Akasaka, S. Ukai, S. Ohnuki, Formation of nanoscale complex oxide particles in mechanically alloyed ferritic steel. Philos. Mag. Lett. **84**(8), 525–529 (2004)
276. Z. Yanushkevich, A. Mogucheva, M. Tikhonova, A. Belyakov, R. Kaibyshev, Structural strengthening of an austenitic stainless steel subjected to warm-to-hot working. Mater. Charact. **62**(4), 432–437 (2011)
277. J.K. Yates, British steel: Innovation in rail steel. Sci. Parliament **53**, 2–3 (1996)
278. c.H. Young, H. Bhadeshia, Strength of mixtures of bainite and martensite. Mater. Sci. Technol. **10**(3), 209–214 (1994)
279. P. Yvon, *Structural Materials for Generation IV Nuclear Reactors* (Woodhead Publishing, 2016)
280. G.G. Zakharova, E.G. Astafurova, The influence of severe plastic deformation by high pressure torsion on structure and mechanical properties of Hadfield steel single crystals. J. Phys. Conf. Ser. **240**(1), 012139 (2010)
281. M.J. Zehetbauer, Y.T. Zhu, *Bulk Nanostructured Materials* (Wiley, 2009)
282. C. Zener, Kinetics of the decomposition of austenite. Trans. Am. Inst. Min. Metall. Eng. **167**, 550–595 (1946)
283. X. Zhang, A. Godfrey, X. Huang, N. Hansen, Q. Liu, Microstructure and strengthening mechanisms in cold-drawn pearlitic steel wire. Acta Mater. **59**(9), 3422–3430 (2011)